Morphological-based Analyses for Parameterizing Symmetry in Radio Galaxies

Mohsen Javaherian ![ORCID], Halime Miraghaei ![ORCID], and Hooman Moradpour ![ORCID]
Research Institute for Astronomy and Astrophysics of Maragha (RIAAM), University of Maragheh, 55136-553, Maragheh, Iran; javaherian@maragheh.ac.ir

Abstract

The morphology of radio galaxies can provide significant clues to describe the formation and evolution of galaxies in the Universe. Here, we aim to extract the morphological parameters of radio galaxies and define symmetry criteria as some of the essential factors of their shape explanations. We employed 67 radio galaxies, which include Fanaroff–Riley type 1 and type 2 galaxies, and their radio images from the FIRST and LoTSS surveys. We developed an automatic segmentation process to extract morphological properties such as the size of objects, eccentricity, and orientation of segmented regions from data sets. Using a maximum likelihood estimator, we show that the distributions of sizes follow a power-law function with exponents of -0.39 ± 0.06 and -0.55 ± 0.05 for the FIRST and LoTSS data, respectively. We found that type 2 radio galaxies have slightly lower eccentricities than type 1. We studied the relationships between size, eccentricity, and redshift in scatter plots. The size of galaxies (kpc^2) demonstrates gently growing trends with increasing eccentricity in their scatter plots. We discussed the possible effect of the redshifts of the galaxies on this result. Depending on the number of segmented regions, we defined symmetry criteria based on proximity to the center of a galaxy in the optical band, eccentricity, orientation, and the quarter (q) of appearance in the image. We found that the mean symmetry obtained for two segmented regions that mainly emerged in two quarters via the condition of $|q' - q''| = 2$ has a higher value than those obtained for other cases.

Unified Astronomy Thesaurus concepts: Radio galaxies (1343); Catalogs (205); Astronomy data analysis (1858)

1. Introduction

Exploring nonthermal and polarized emissions of radio galaxies provides a unique way of understanding active galactic nuclei (AGNs). The evolution of AGNs, the complex interconnection with their medium, and the physical processes around the supermassive black holes can be studied delicately by consideration of the properties of radio galaxies. These include a wide range of measurements from a very-high-resolution very long baseline interferometry (VLBI) observations at parsec scales to very deep observations of the large-scale environment at a few megaparsecs. The radio continuum spectrum, luminosity, spectral index, morphology, and their correlations with properties of AGNs at other frequencies are also considered (Heckman & Best 2014; Hardcastle & Croston 2020).

In terms of morphology, investigations of galaxy maps in radio passbands lead to some primary but growing morphological classifications that help to fabricate well-structured theories for the formation and evolution of AGN jets. Fanaroff & Riley (1974; FR hereafter) proposed the first classification scheme for radio galaxies based on the location of the peak intensity and the extent of the radio jets. They classified radio sources into two groups, mainly known as FRI and FRII radio galaxies. In the FRI class, the profile of intensity peaks near the center while it is near the edge in the FRII class. In recent studies, compact radio sources were added to this category as a third class of FR0 radio galaxies (Baldi et al. 2015).

Previous studies show that there are correlations between radio morphology and other properties of galaxies including their environment. While FRI radio galaxies are associated with a dense environment and low excitation index, FRIIs prefer a low-density environment and high-excitation AGN activity (Hill & Lilly 1991; Baum et al. 1995; Gendre et al. 2010, 2013). Their host galaxies are also different (Baum et al. 1992; Heckman et al. 1994; Baum et al. 1995; Govoni et al. 2000; Scarpa & Urry 2001), however, much of the differences are removed when the samples are corrected for the excitation index (Miraghaei & Best 2017). Bent-tailed, wide-angle-tailed (WAT), and head-tailed (HT) radio galaxies as subclasses of FRIs are efficiently used to identify overdensities because their jets are bent due to the galaxy movement within a group or a cluster (Blanton et al. 2000, 2001; Dehghan et al. 2014; O'Brien et al. 2016). The main properties of the radio sources with compact morphologies such as FR0, gigahertz peaked-spectrum (GPS), and compact steep-spectrum (CSS) are still discussed in the literature as they may fundamentally constitute different populations of radio galaxies (O'Dea & Saikia 2021, and references therein).

As new high-resolution and sensitive radio surveys have been arriving, the need for revisiting these morphological classifications is inevitable. In addition, machine-learning techniques (e.g., Aniyan & Thorat 2017; Lukic et al. 2018; An et al. 2018; Tang et al. 2019; Sadeghi et al. 2021) have been applied to introduce automatic methods for morphological-based classification of radio galaxies. In terms of machine-learning algorithms and image analysis which are applied to LOFAR, a composition of novel models is exploited to involve optical features of host galaxies and morphological parameters in their classifications (Alegre et al. 2022; Barkus et al. 2022). Moreover, some articles employed dimensionality reduction procedures combined with machine-learning models in supervised (Mosavi et al. 2021) and unsupervised (Mostert et al. 2021) classifications. The classical classifications based on the location of the peak intensity are updated to account for more complex structures in the maps of radio galaxies. In this

regard, Mingo et al. (2019) showed a large population of FRI-classified radio galaxies with core-dominant morphology restarting FRIIs. They also discovered some complex structures which cannot be classified within the current definition of radio galaxy classifications. Sources without classification are also reported by Miraghaei & Best (2017). Due to the diversity of galaxy morphologies (e.g., the wide variety of "X-shaped," "S-shaped," and "C-shaped" radio galaxies) observed via modern telescopes, Rudnick (2021) has summarized the advantages of creating an evolutionary catalog based on a #tag system to make classifications understandable, applicable, and flexible. Therefore, introducing novel methods for the investigation of radio maps is necessary to quantify morphologies.

The morphological and intensity analyses of radio galaxies have become the foundation of many studies. Baum & Heckman (1989) found differences in the spatial expansion and radio luminosity between FRI and FRII galaxies. They discovered that galaxies larger than 200 kpc tend to orient in the direction of the minor axis of the host galaxy. Schoenmakers et al. (2000) found that the outer pair is brighter than the smaller inner pair by analyzing a sample of sources consisting of a pair of double-lobed galaxies along their axis. Golden-Marx et al. (2021) statistically investigated the opening angles of bent sources and their orientations relative to the cluster centers.

Historically, many articles used the term "symmetry" for radio sources observed as compact or medium-symmetric objects (Readhead et al. 1996a, 1996b; Augusto et al. 2006). This kind of classification was often done manually based on the source brightness (Bridle et al. 1994). The symmetry of these large structures was not determined automatically by the definition of a morphological-based quantity. Bera et al. (2020) studied the symmetrical morphology of some exotic features such as X-shaped and Z-shaped radio galaxies based on the brightness of lobes and the angle between the minor and major axis of galaxies. Most papers focused on asymmetry and its relationship with the physical parameters of galaxies and/or their environment. For example, Lara et al. (2004) discussed three feasible reasons causing the apparent asymmetry in radio galaxies. Laing et al. (1999) and Hocuk & Barthel (2010) used luminosity and orientation, respectively, to discuss the asymmetries of radio structures. Moreover, asymmetry manifests itself in flux density maps, spectral index, and the size of lobes (Taylor et al. 1996a, 1996b; Dennett-Thorpe et al. 1999; Augusto et al. 2006). The detection of asymmetries in the maps of radio galaxies is also reported in the literature (Gopal-Krishna & Wiita 2004). In this regard, there are FR hybrid radio galaxies which are FRI on one side and FRII on the other side. These asymmetries can be due to orientation and line-of-sight effects (Harwood et al. 2020), can be the result of the interaction of the jets with their environment, or they may have a more fundamental explanation (Gopal-Krishna & Wiita 2000; Gawroński et al. 2006; Cegłowski et al. 2013). According to the relative position of each radio intensity peak, some articles investigated asymmetry by exploiting the fractional separation difference to allocate physical properties to this index (Banhatti 1980; Arshakian & Longair 2000; Jimenez-Gallardo et al. 2019).

Reviewing the articles regarding the symmetrical and/or asymmetrical properties of galaxies implies that there is not an effective method combining all symmetrical parameters in their proposed techniques. Because of the lack of a thoroughgoing robust algorithm, we developed a method for automatic parameter extraction related to symmetry in radio galaxies.

We present an approach based on the image processing technique to carry out the morphological classification of galaxies and their differences by considering parameters related to symmetry. To do this, we provide a package including preprocessing, segmentation, and parameter extraction procedures. The paper is organized as follows: the radio galaxy data sets are explained in Section 2. The method of morphology analysis using image processing techniques is described in Section 3. We present the results and discuss the symmetry of radio galaxies in Section 4. Summary and concluding remarks are given in Section 5.

2. Description of the Radio Data Set

We used the FR radio galaxy catalog presented in Miraghaei & Best (2017), and the extended source catalog from LOFAR Two-Meter Sky Survey (LoTSS) Data Release 1 (DR1; Shimwell et al. 2019) presented in Mingo et al. (2019).

The catalog of Miraghaei & Best (2017) is constructed based on the NVSS (Condon et al. 1998) and FIRST (Becker et al. 1995) radio source surveys at 1.4 GHz with the identifications of the host galaxies based on the Sloan Digital Sky Survey (SDSS) RD7 spectroscopic sample (Best & Heckman 2012). The catalog covers $\sim$8200 degree^2 of the SDSS and lists 1329 radio galaxies with extended morphologies as FRI, FRII, hybrid, and unclassified. A label of certain or uncertain is appointed to each source based on the data quality for their classifications. The complex structures are labeled as WAT, HT, and double–double (DD) sources.

The catalog of Mingo et al. (2019) is constructed based on LoTSS DR1, observed at the full resolution ($\sim$6″) and sensitivity ($<$0.1 mJy beam^{-1}) of the Dutch LOFAR high band antennas at 150 MHz. LoTSS DR1 contains 318,520 sources over 424 degree^2 of the Northern sky. A sample of 5805 extended radio-loud AGNs has been identified and classified as FRI, FRII, and intermediates, which are listed in this catalog. Sources are also labeled as small if their angular sizes were below the resolved criteria introduced by Shimwell et al. (2019). Therefore, less reliable classifications are appointed by this label. Complex structures such as WAT and DD are also determined in the catalog. Sources labeled as intermediate include those that are not FRI or FRII such as hybrid FRs, core-dominated sources (core-Ds), or fuzzy blobs. Sources that meet none of the criteria are considered unclassified. For an overview of radio AGNs and recent LOFAR results, the reader can refer to Hardcastle & Croston (2020).

The sky coverage of the two catalogs is presented in Figure 1. LoTSS provides a deeper radio AGN sample (median redshift of $\sim$0.5) compared to the FIRST/NVSS catalog (median redshift of $\sim$0.2) due to the higher sensitivity of the antennas. Mingo et al. (2019) discarded all sources with a total flux of less than 2 mJy in the LOTSS catalog while a lower threshold of 40 mJy is used for the FIRST/NVSS catalog. The dense core of LOFAR produces a very high density of measurements within 2 km, which provides excellent uv coverage for the LoTSS in comparison with those of FIRST/ NVSS. This leads to better detection for the extended emissions. The low surface brightness extended emissions are missed by the FIRST/NVSS catalog. Finally, the average spectral index $\alpha \sim 0.7$ ($f \propto \nu^{-\alpha}$, wherein f and ν are the flux density of the radio source and the frequency of the observations, respectively) for jetted AGNs shows that these sources are brighter at low frequencies. The benefit of
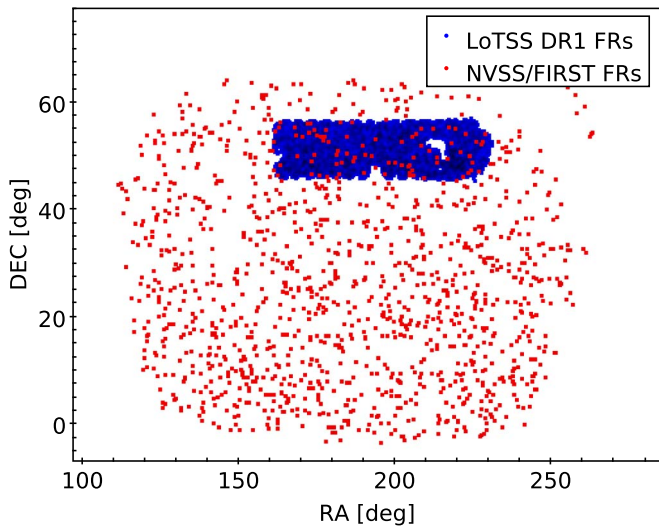
Figure 1. The sky coverage of the extended source catalogs taken from FIRST/NVSS (red) and LoTSS (blue) is described in Section 2.

observing radio jets at low frequencies is that we can detect synchrotron emissions from old electrons. These emissions cannot be detected at high radio frequencies due to spectral aging. All of these explain the remarkable difference in the number density of sources between the two catalogs in Figure 1.

We exploited the images obtained from the FIRST cutout server with a higher resolution ($\sim 5''$) than the resolution of the NVSS images ($\sim 45''$) to get more details about the morphologies of the sources. The noise level of the images is about 0.15 mJy. Also, we used the LoTSS DR1 image cutout service to extract the radio images. The radio images are mapped at two classes of high ($\sim 6''$) and low ($\sim 20''$) resolution. High-resolution radio images are selected in this work. The resolution is comparable with the resolution of FIRST while lower surface brightness extended sources are better detected in LoTSS. The pixel sizes are $1''.8$ and $1''.5$ for FIRST and LoTSS, respectively.

The two catalogs have been cross-matched to construct a sample of 67 FR-classified radio galaxies. As it is shown in Figure 1, about 80 sources from the FIRST/NVSS catalog overlap with LoTSS (including those in the border regions). To find true candidates matched from both catalogs, we first find the nearest matched sources, then visually inspect and check the images to make sure that they are identical. A sample of 72 sources was selected as true matches. Five sources out of 72 had been labeled as hybrid (2) or unclassified (3), which we discarded from the target sample. A subsample of 67 sources was finally used in this study. According to Miraghaei & Best (2017), this subsample contains 34 FRIs including 20 certain FRIs, four of which are listed as WAT sources, and 14 uncertain FRIs. This also contains 33 FRIIs including 27 certain and six uncertain FRIIs. These sources are classified by Mingo et al. (2019) as 38 FRIs including 12 WAT, nine FRIIs, 27 intermediates, and one remains unclassified. The resolution limitation is crucial in the classification of radio sources. Mingo et al. (2019) labeled sources as small with radio size $< 27''$ or radio size $< 40''$ with $d_1 + d_2 < 20''$ where d_1 and d_2 are the brightest peaks of emissions on each side of the source. They also discarded all sources with total sizes of $<12''$ (two to three times the resolution of the surveys) as those are too small to be classified as an FR radio galaxy. 15 sources, mostly FRIs, are labeled as small. A major difference between these two classifications is the number of FRIIs and intermediate sources. Some FRIIs reported in Miraghaei & Best (2017) are classified as FRIs in Mingo et al. (2019), but they are all labeled as small. Only two of them show very diffused extended emissions detected by LOFAR antennas which reveal their correct FR class. On the other hand, some FRIs are classified as intermediate by Mingo et al. (2019). This is also due to the high sensitivity of the survey to detect complex structures. This study aims to define a parameter to evaluate the morphological properties of the extended radio galaxies regardless of their classifications. Therefore, mismatches between different classification methods are not a big issue in this study. This analysis is based on the classifications presented by Miraghaei & Best (2017), while we used image data from both catalogs. An example of original data of an FRI galaxy recorded by both FIRST and LoTSS is presented in Figure 2, panels (a) and (e), respectively. Also, an example of original data of an FRII galaxy recorded by both FIRST and LoTSS are shown in Figure 3, panels (a) and (e), respectively.

3. Description of the Method

Here, we introduced an automatic segmentation algorithm to segregate objects and extract their characteristics in radio galaxy images. Our method involves the preprocessing, segmentation procedure, and image analysis to find the intensity-weighted centroid (IWC), eccentricity, and orientation for defining the symmetry criteria of galaxies.

3.1. Preprocessing

In this level, first, the origin of each image is placed at the center of the galaxy that appeared in the visible spectrum. Then, the intensities of pixels in each image are normalized to the maximum brightness of the related image. To assure that the data analysis is fulfilled within the minimum threshold of noise, a denoising procedure is applied to each image. For wavelet denoising in a selective way, it is necessary to find the threshold coefficients using the global default threshold, which is obtained by $\sigma . \sqrt{2 \log n}$, wherein σ and n are the noise variance and sample size, respectively (Donoho & Johnstone 1994; Donoho 1995). To reconstruct an unknown one-dimensional noisy function g, it is assumed that we deal with the noisy series as $s_i = g(h_i) + e_i$, wherein $i = 1,...,n$ (number of points with equally spaced range), and $h_i = i/n$. The coefficients e_i are extracted from an independent and identically distributed normal function $N(0, \sigma^2 = 1)$. The aim is to find the reconstructed denoised function $\hat{g}$ from the estimated sample in the wavelet domain. The empirical wavelet coefficients of $\hat{g}$ must be less than or equal to the coefficients of g to guarantee that $\hat{g}$ is smoother than g (Donoho 1995). So, we must minimize the mean-squared error that can be expressed as the following risk function, R

$$R(g, \hat{g}) = \frac{\sum_{i=1}^{n} E[g(h_i) - \hat{g}(h_i)]^2}{n}. \tag{1}$$

One of the approaches for solving this minimization problem employed a spatially adaptive method based on selective wavelet reconstruction. Donoho & Johnstone (1994) found an approximated relation for wavelet-based
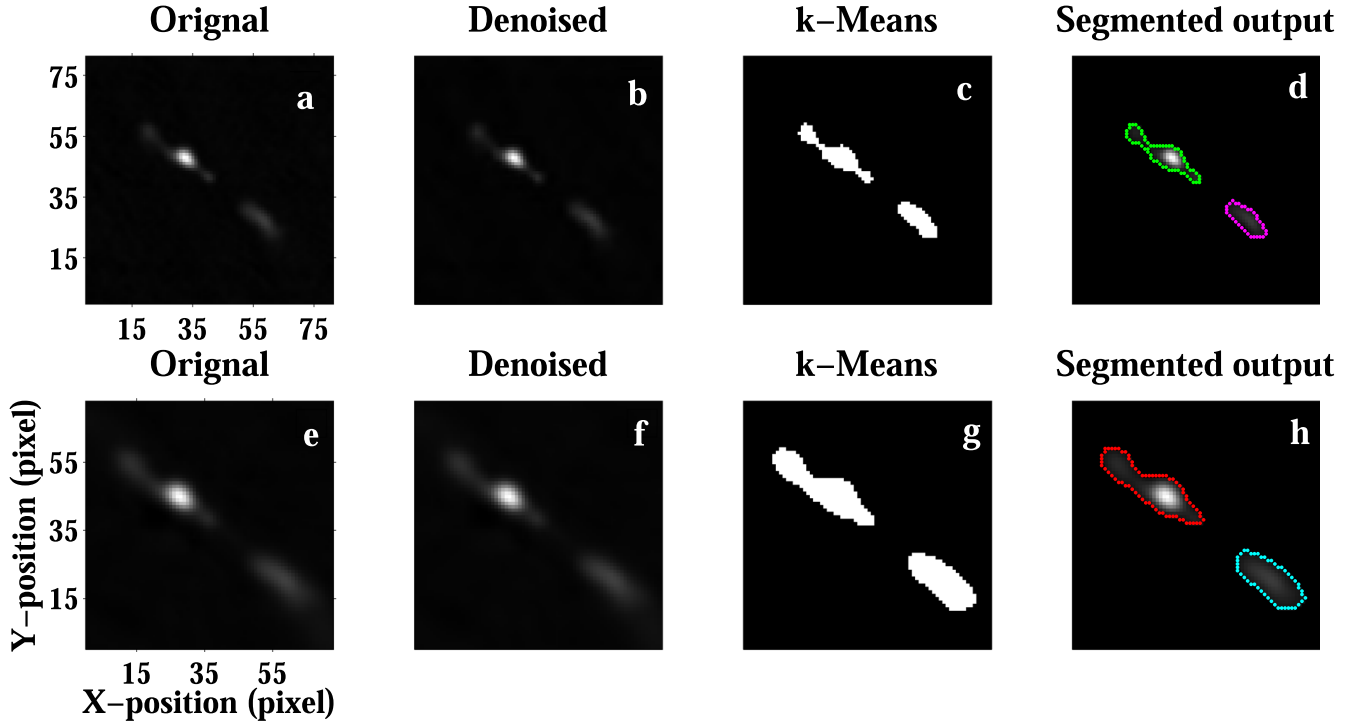
Figure 2. Segmentation process of an FRI radio galaxy with ID number 1 (Table 1). Top: (a) the original (cropped) image from FIRST data with lower resolution (signal-to-noise ratio (S/N) = 32.82 ± 0.86), (b) the denoised image with S/N = 32.98 ± 0.87, (c) the logical output of the *k*-means algorithm, and (d) the segments of the FRI radio galaxy. Bottom: (e) the original (cropped) image from LoTSS data with higher resolution (S/N = 31.86 ± 0.22), (f) the denoised image with S/N = 31.86 ± 0.22, (g) the logical output of the *k*-means algorithm, and (h) the segments of the FRI radio galaxy.

near-ideal reconstruction when we just deal with original data with no additional information about *g*. This formula is as follows

$$R_{n,\sigma}(g, \hat{g}) \leqslant (2\log n + 1)\left(\Re_{n,\sigma}(sw, g) + \frac{\sigma^2}{n}\right), \qquad (2)$$

where $\Re_{n,\sigma}(sw, g) = \mathcal{O}\left(\frac{\sigma^2 \log n}{n}\right)$, and *sw* is the abbreviation of selective wavelet reconstruction. Thus, by using this approximation, this method provides a good estimation for optimizing the risk function that can be applied to two-dimensional noisy data (Gupta et al. 2013). The S/N $= \frac{\sigma^2_{signal}}{\sigma^2_{noise}}$ is computed for each image before and after denoising. Among the original image and the denoised one, each one that has the greater S/N is considered as input for the next step. For the denoised outputs of FIRST and LoTSS data, see Figures 2 and 3, panels (b) and (f).

3.2. Segmentation

Our segmentation process involved two main steps: histogram-based intensity thresholding and the *k*-means clustering segmentation algorithm. In the first step, the intensity threshold is determined by the normalized intensities that appeared in the second bin of the histogram. The first bin includes the countless pixels with galaxies of lower brightness that must be omitted from the segmentation process. So, the beginning of the second bin is the lower limit for the intensity thresholding. The semilogarithmic histogram of normalized intensities obtained for the denoised FRI radio galaxy with ID number 1 recorded by FIRST is demonstrated in Figure 4

(upper panels). In the same way, the semilogarithmic histogram of normalized intensities is obtained for the denoised FRII radio galaxy with ID number 41 recorded by LoTSS (Figure 4, lower panels). The first bins of both histograms are representative of dark pixels in the images, and so, the second bin is assigned as the lower limit of intensity thresholding in segmentation. The interested reader can refer to Stucki et al. (2000), Raju & Bromage (2006), Krista & Gallagher (2009), Wedemeyer-Böhm & Rouppe van der Voort (2009), and Hamada et al. (2018) for astronomical applications of intensity histogram-based approaches.

In the next step, *k*-means clustering, as an unsupervised iterative nondeterministic method, is employed for image segmentation. Pixels with intensities smaller than the lower limit of the histogram (second bin) are excluded from the segmentation procedure and the remaining ones are inserted into the next step as the input. In this algorithm, *l* features are grouped in *k* clusters. Each feature is classified into a certain cluster with the criterion of the nearest mean. In simple terms, imagine that the intensity of pixels and their locations in the image are mapped to three-dimensional feature space. Since the intensities are the third dimension, those pixels that have similar brightness are placed in the same clusters depending on their mean distances. For a mathematical explanation of *k*-means (e.g., Inbarani et al. 2020), suppose that we have *l* features (pixels) as the set of $Z = \{z_1, z_2,...,z_l\}$. Since the number of clusters is determined by the user at the beginning of running the code, we determined four clusters of intensities for *k*-means segmentation using trial and error including all pixels of the object. First, the positions of the *k* clusters (here, *k* is four) in the feature space is randomly selected as the initial centers of clusters *c* in the feature space. Then, the cluster of each feature is determined by the following
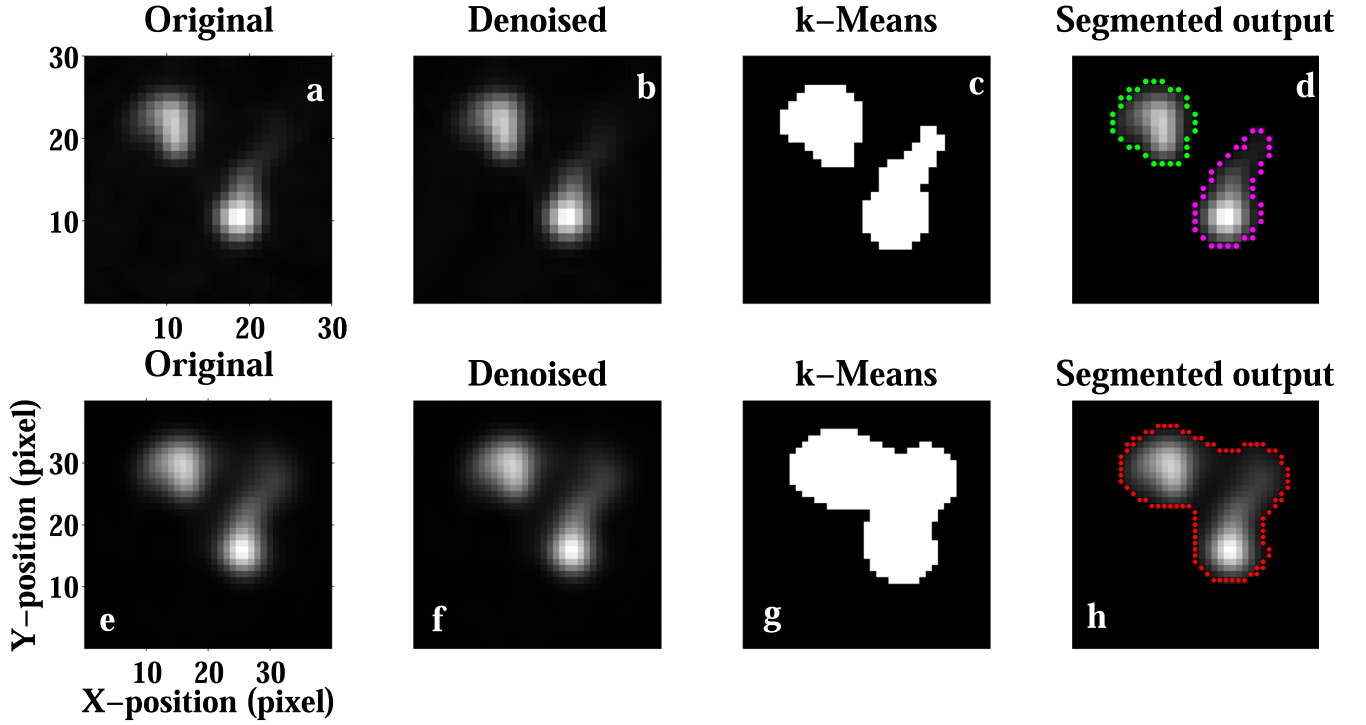
Figure 3. Segmentation process of an FRII radio galaxy with ID number 41 (Table 2). Top: (a) the original (cropped) image from FIRST data with lower resolution (S/N = 30.8 ± 1.2), (b) the denoised image with S/N = 30.8 ± 1.2, (c) the logical output of the k-means algorithm, and (d) the segments of the FRII radio galaxy. Bottom: (e) the original (cropped) image from LoTSS data with higher resolution (S/N = 29.50 ± 0.21), (f) the denoised image with S/N = 29.51 ± 0.21, (g) the logical output of the k-means algorithm, and (h) the segments of the FRII radio galaxy.

objective function, D

$$D = \sum_{j=1}^{k}\sum_{i=1}^{l}||z_i^{(j)} - c_j||^2. \qquad (3)$$

The convergence of the objective function is achieved when the optimized solution is iteratively computed for features. The iteration is stopped when there are no changes in the cluster centers (Khan & Ahmad 2004; Yousefzadeh et al. 2015). Thus, each pixel belongs to its cluster, which is specified as a segregated region. Note that the minimum size for segmented regions is considered to be 12 pixels, and the smaller ones are removed. This is about 2–3 times the resolution of the surveys. Moreover, larger regions placed far away from the center of the image are automatically removed, where their IWCs are out of the circle centered in the center of the image, while the circle diameter is equal to a side of the image. In Figure 2, panels (c) and (g) show the outputs of k-means clustering applied to FRI galaxies taken by FIRST and LoTSS, respectively. Also, in Figure 3, panels (c) and (g) show the outputs of k-means clustering applied to FRII galaxies taken by FIRST and LoTSS, respectively. The segmentation outputs with edges displayed in original images are shown in Figures 2 and 3, panels (d) and (h).

3.3. IWC, Orientation, and Eccentricity

After segregating objects, the region(s) with their original intensities remain. We used the central moments of the image to find the IWC, eccentricity, and orientation of each region (Noori et al. 2019; Tajik et al. 2023). For an image $F(x, y)$, the central moments μ_{rs} are given by the following formula

$$\mu_{rs} = \sum_x\sum_y(x - X_{IWC})^r(y - Y_{IWC})^s F(x, y), \qquad (4)$$

where $X_{IWC} = \frac{m_{10}}{m_{00}}$ and $Y_{IWC} = \frac{m_{01}}{m_{00}}$ are the coordinates of the IWC that can be obtained by

$$m_{rs} = \sum_x\sum_y x^r y^s F(x, y). \qquad (5)$$

According to this, the zero-order moment m_{00} has the definition of the region area A. Having the centroid, the quarter of the target is obtained in Cartesian coordinates. The orientation ω of the object relative to the positive x-axis can be expressed by

$$\omega = \frac{1}{2}\arctan\left(\frac{2\mu_{11}}{\mu_{20} - \mu_{02}}\right). \qquad (6)$$

We should mention that the value of angle ω is in the range of -90 to 90. Using orientation and fitting the bounding box of the object, the major axis of the shape (a) and then its minor axis (b) can be computed. So, the eccentricity ε is found by

$$\varepsilon = \sqrt{1 - \frac{b^2}{a^2}}. \qquad (7)$$

The parameter ε always ranges from 0 to 1. For a circle, the parameter $\varepsilon = 0$; and the parameter $\varepsilon = 1$ is representative of a line. Using the error propagation approach, the relations for computing error ranges of the orientation and eccentricity are explained in the Appendix.

4. Results and Discussions

As we hinted in Section 3, we applied the segmentation procedure to radio images after the normalizing and denoising steps. When the target is segregated from the background, the morphological parameters (size, IWC, eccentricity, and

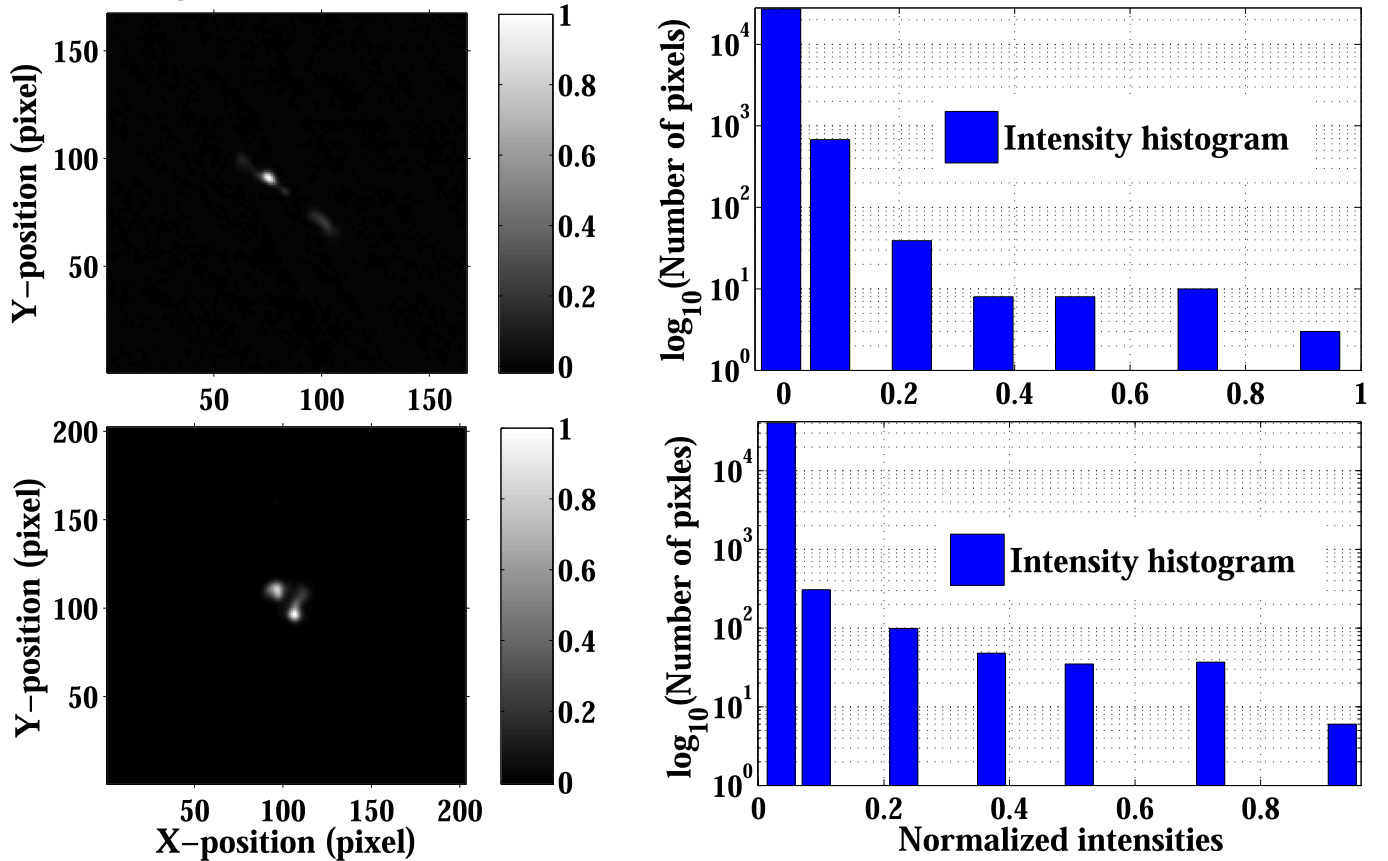## Denoised images with normalized intensities

Figure 4. We present a denoised image of an FRI radio galaxy in its original size from FIRST data with ID number 1 (upper left panel) with a histogram of normalized intensities in a semilogarithmic scale (upper right panel). The normalization process is fulfilled by dividing all intensities by the maximum brightness of the image. Also, we present a denoised image of an FRII radio galaxy in its original size from LoTSS data with ID number 41 (lower left panel) with a histogram of normalized intensities in a semilogarithmic scale (lower right panel). The first bin of the histogram includes the dark pixels of the image that must be omitted from the next steps of the segmentation process.

orientation) of the sources are obtained. We should note that a line-of-sight jet may display different properties than what it is due to relativistic beaming and projection effects. For example, Harwood et al. (2020) showed that FRII radio galaxies can be seen as FR hybrids due to their special orientations. To correct this effect, we need to find the contribution of beamed sources, which is different in each catalog. Mazoochi et al. (2022) have discussed it for a sample of FRIIs selected from the catalog provided by Miraghaei & Best (2017). They showed that even for the core of FRIIs (compact component), beamed sources constitute 6%–30% of the sample. In comparison, the extended radio sky is less influenced by relativistic beaming than the compact sky. Thus, we expect even lower contamination by beamed sources in this work. In the following, we study the frequency distribution of these properties of regions and their relationships as scatter plots.

4.1. Size–, Orientation–, and Eccentricity–Frequency Distributions of Segmented Regions

The size distributions of radio galaxies for FIRST and LoTSS data are shown in Figures 5 and 6, respectively. These plots present the physical sizes of the segmented regions. Their corresponding angular sizes are well distributed above two times the resolution of the surveys. As discussed in Section 2, a threshold of 12 pixels removes segmented regions below two

times the resolution of the surveys. Therefore, the resolution limitations do not influence the results for the physical sizes.

Using the maximum likelihood estimator (MLE: Clauset et al. 2009) method, power-law functions are fitted to the probability size distributions of segments (for astronomical applications of MLEs in fitting the power-law distributional model to data and its details, the reader can refer to Arish et al. 2016; Javaherian et al. 2017; Moradhaseli et al. 2021). In Figure 5, a power-law model (black line) with an exponent of $\gamma = -0.39$ is fitted to the empirical FIRST data (blue line). In Figure 6, the exponent of the power-law fit (black line) for the frequency distribution of sizes in LoTSS data (red line) is obtained to be $\delta = -0.55$. Due to the greater slope of the sizes in the distribution of LoTSS data, it can be said that small-scale structures have a more significant contribution to the distribution. In fact, the detection of small-scale structures in LoTSS data is more than those obtained for FIRST data. Since a wide range of redshifts is used, physically small sources at high redshifts are missed in these plots. The deviations from the power-law model in the tail of the right side of Figure 6 pertain to the formation of rare events on very large scales. There is a relation for the standard error on the exponent of the power-law model $\sigma_{\text{power-law model}}$ as follows

$$\sigma_{\text{power-law model}} = \frac{|\text{magnitude value of the exponet} - 1|}{\sqrt{\text{number of data points}}}. \quad (8)$$
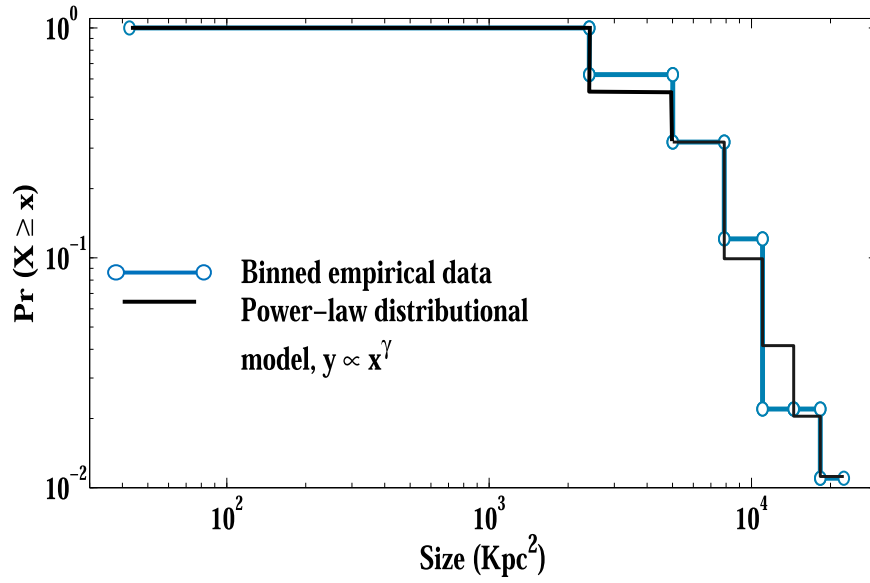
Figure 5. The power-law model (black line) is fitted to the size–frequency distribution of FIRST data (blue line) in a log–log scale. Using the MLE method, the exponent (γ) of the probability distribution function is obtained to be -0.39 ± 0.06. The vertical and horizontal lines are representative of vertical and horizontal error bars extracted from the fitted model.
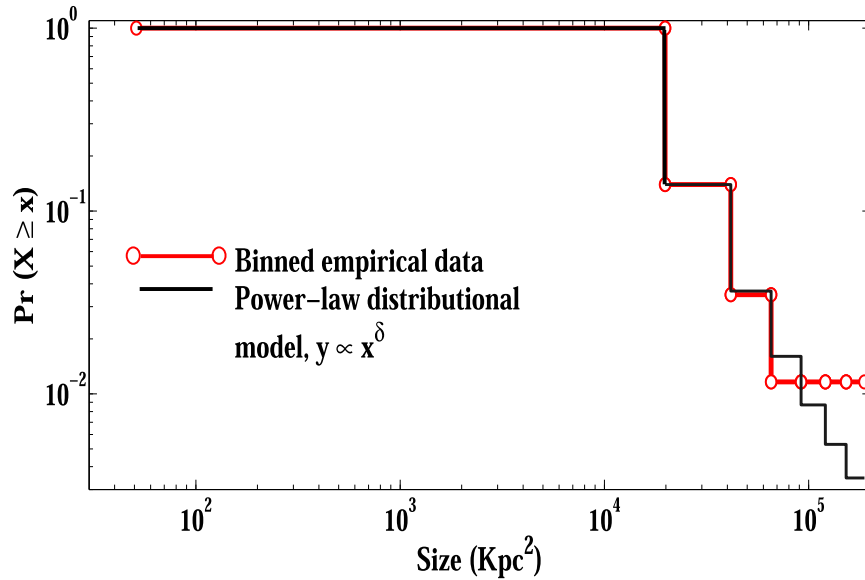
Figure 6. The power-law model (black line) is fitted to the size–frequency distribution of LoTSS data (red line) in a log–log scale. Using the MLE method, the exponent (δ) of the probability distribution function is obtained to be -0.55 ± 0.05. The vertical and horizontal lines are representative of vertical and horizontal error bars extracted from the fitted model.

Since we have 91 and 85 points for segmented regions extracted from the FIRST and LoTSS data sets, respectively, the standard errors on the exponent of the power-law model are obtained to be 0.06 and 0.05 for the FIRST and LoTSS data, respectively. The use of Equation (8) requires one condition, in that our data must be bounded to a range above a given threshold (Clauset et al. 2009), which we exploited in the segmentation process.

Using the formulas in Section 3.3, the orientations and eccentricities of segments are computed. The frequency distributions of orientations and eccentricities are shown in Figures 7 and 8, respectively. The histograms of orientations show thoroughly random patterns. There is also no difference between type 1 and type 2 radio galaxies in these plots. They are

consistent with a random distribution of radio galaxies along our line of sight. The eccentricity distributions show negative skewness consisting of values ranging from zero to one. Circle-like shapes have values close to zero, and the eccentricity increases toward one when it approaches an elongated ellipsoid. A large number of radio segments show eccentricities larger than 0.7. Type 2 radio galaxies have slightly lower eccentricities than type 1. This denotes that FRI segments have more elliptical shapes than FRII segments.

We used Kolmogorov–Smirnov (K-S) tests to find the probabilities of the differences. This statistical test can compare cumulative distributions of two parameters. The values of the probabilities P report the levels at which the null hypothesis is rejected. We found $P > 90\%$ and $P > 95\%$ for the FIRST and
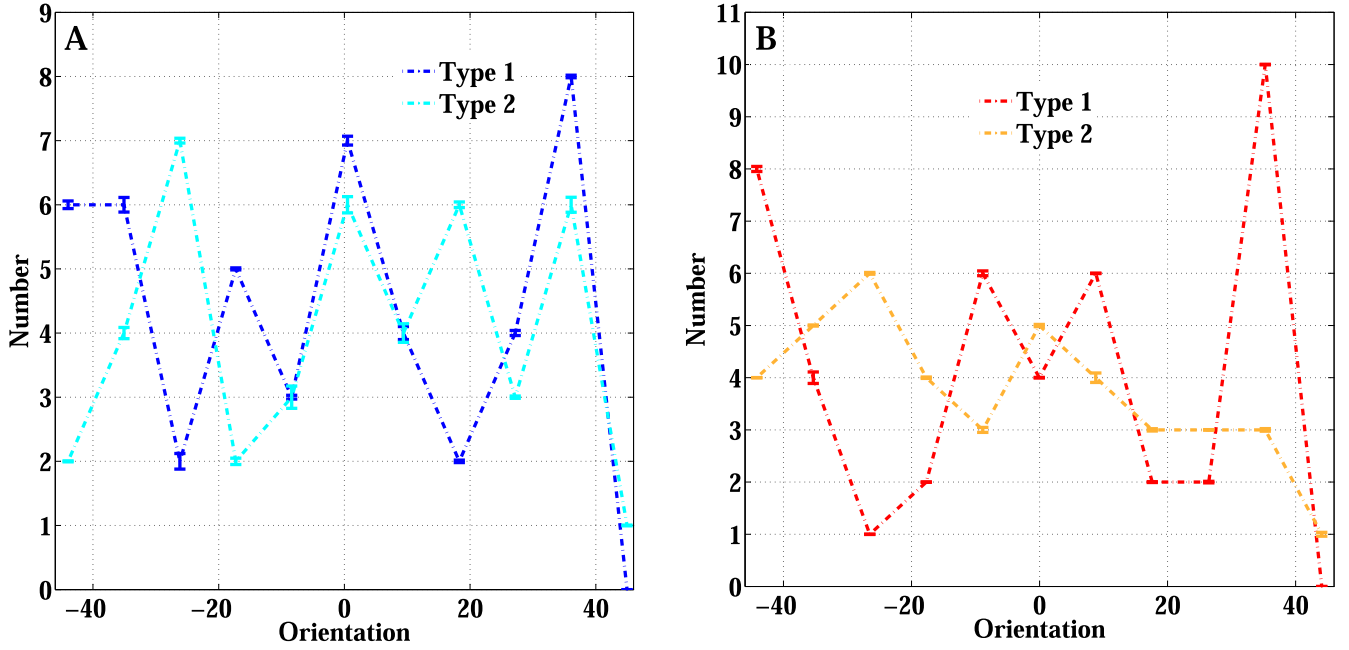
Figure 7. The orientation distributions of FIRST data (left panel) and LoTSS data (right panel) with their error bars. Type 1 galaxies are displayed by the blue and red colors for the FIRST and LoTSS data, respectively. Type 2 galaxies are displayed by the cyan and orange colors for the FIRST and LoTSS data, respectively. It can be seen that there are correlated behaviors between graphs related to type 1 galaxies in both data sets and also between graphs when type 2 galaxies are compared in both data sets. The maximum number of orientations appears around 30° for type 1 galaxies in both data sets.
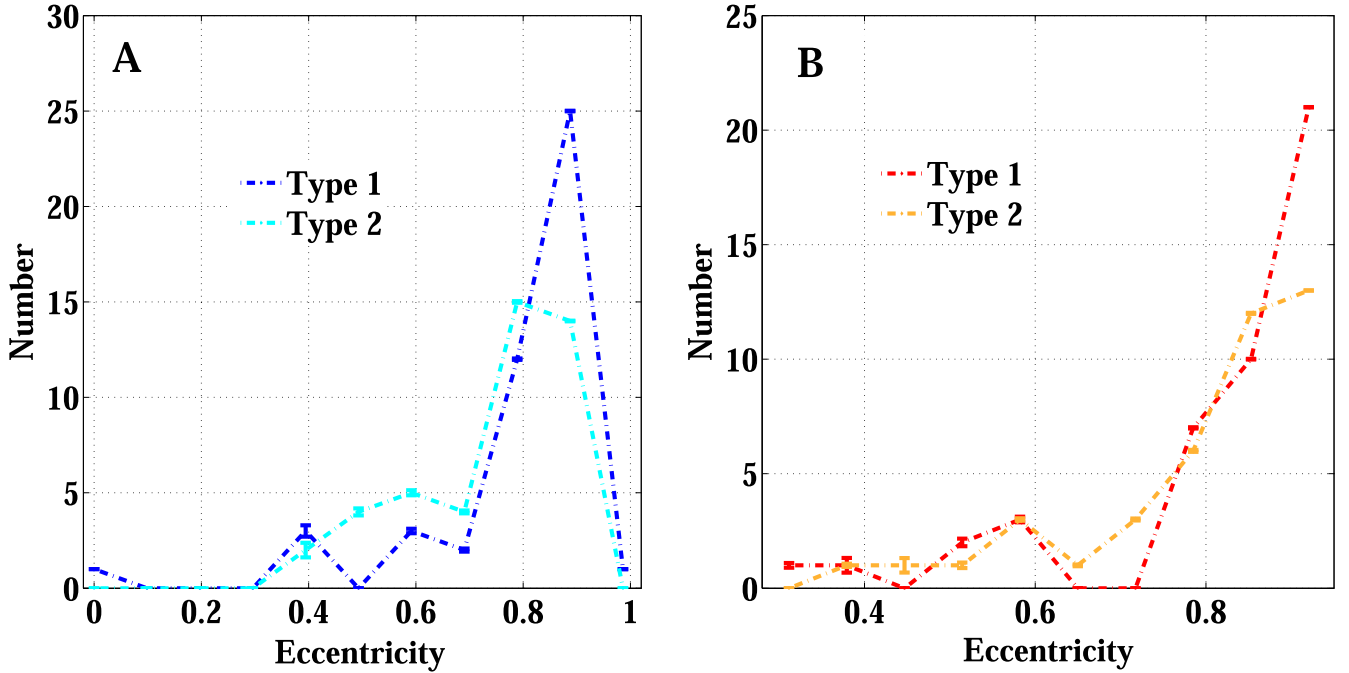
Figure 8. The eccentricity distributions of FIRST data (left panel) and LoTSS data (right panel) with their error bars. Type 1 galaxies are displayed by the blue and red colors for the FIRST and LoTSS data, respectively. Type 2 galaxies are displayed by the cyan and orange colors for the FIRST and LoTSS data, respectively. It can be seen that there are correlated behaviors between graphs related to type 1 galaxies and also type 2 galaxies. The maximum number of eccentricities ranges from 0.8 to 1 for both types of galaxies.

LoTSS data, respectively. Therefore, the difference is significant at $\sim 2\sigma$. To ensure that errors in the classification do not affect on this result, we repeat the analysis by making a lower cut at $20''$ where the classification is more reliable, according to Miraghaei & Best (2017). Below this limit, the result may be contaminated by the resolution limitations. Thus, we compare FRIs with FRIIs. The previous results have been replicated. We found FRIs have higher eccentricities than FRIIs

with $P > 99\%$ for the FIRST data and $P > 90\%$ for the LoTSS data. Therefore, we conclude that our result is not affected by resolution limitations. There is a piece of evidence that shows FRIs are in denser environments compared to FRIIs (Hill & Lilly 1991; Gendre et al. 2013; Miraghaei & Best 2017; Croston et al. 2019) as we discussed in Section 1. Therefore, higher eccentricities in FRIs compared to FRIIs may be the result of the interaction of radio jets with the dense regions in
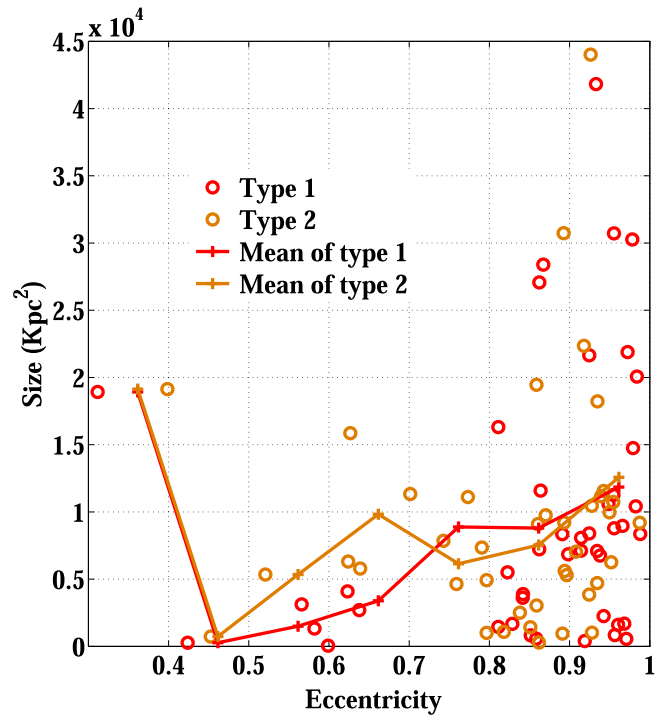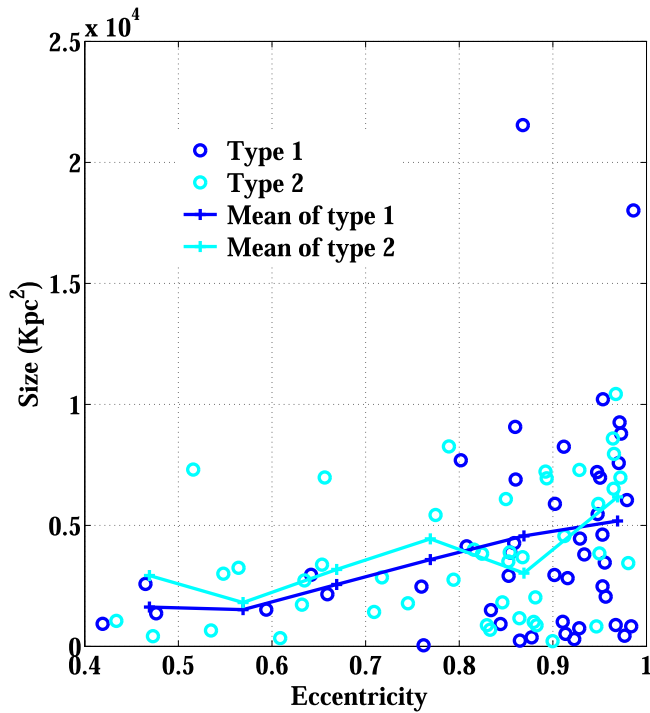
Figure 9. The relationship between the size of galaxies (kpc^2) and their eccentricity for mean values (shown by a +) of each bin (0.4, 0.5, etc.) for the FIRST and LoTSS data are demonstrated in the left and right scatter plots, respectively. The blue circles (with a whole mean of 4313 ± 64) and cyan circles (with a whole mean of 3806 ± 41) belong to type 1 and type 2 galaxies, respectively, in the FIRST data. The red circles (with a whole mean of 9735 ± 148) and orange circles (with a whole mean of 9259 ± 137) belong to type 1 and type 2 galaxies, respectively, in the LoTSS data.

their surroundings. It is also well known that FRI and FRII lobes have different physics and evolve differently (e.g., Kaiser & Best 2007; Laing & Bridle 2014; Hardcastle & Krause 2014). Therefore, the differences in eccentricity could be the result of some intrinsic differences. Accurate consideration is needed to get robust results, such as removing the effect of stellar mass and redshift that impose biases on the data. For this paper, we focus on the description of our method and presenting the technical results. We also compare size (area in kpc^2), distance to the center (kpc), and the redshifts of the type 1 and type 2 segments. No significant differences have been found for these properties.

4.2. Relationships between Size, Eccentricity, and Redshift

Scatter plots of the region sizes (kpc^2) versus eccentricity for the FIRST and LoTSS data sets are displayed in Figure 9 in the left and right panels, respectively. The solid lines show the mean values of the sizes in each bin of eccentricity for each type of galaxy. The plots show that the size of regions increases with increasing eccentricity. Regions with larger eccentricities are more scattered in size. On the other hand, less scattering in size is clear at lower eccentricities. This could be due to the anisotropic nature of radio jets or the effect of the environment on the radio jets, as the jets grow to larger sizes. To explore this more, we plot each property versus redshift. The relation between the size of segmented regions and redshift is shown in Figure 10. We also plot the distance of the IWC from the center (kpc) of these sources (center of images) versus redshift in Figure 11. It can be seen that this property illustrates an increasing trend with redshift. These redshift dependencies are due to the selection effect in our sample. Since our sample is not complete at radio frequencies, low-power radio sources are missing at high redshifts. Therefore, only high-power extended

radio galaxies that are larger (either in terms of the size of the extended emission or the radial size to the optical center of the galaxy) can be detected at high redshifts. To ensure that this selection effect does not influence our results for the size–eccentricity trend, we plot eccentricity versus redshift in Figure 12. There is no relation between these two properties, which means the result of eccentricity is not affected by selection bias due to incomplete sampling. We have also investigated this by comparing a sample of high-redshift sources with a sample of low-redshift sources. Figure 13 shows size versus eccentricity for our sample divided into two subsamples of high- and low-redshifts for the FIRST (left-hand panel) and LoTSS (right-hand panel) data. The plot presents the same result as Figure 9 for each redshift bin. To keep the subsamples rich enough to achieve a significant result, type 1 and type 2 sources have not been investigated separately in Figure 13. This issue cannot influence our result because no difference has been found between the type 1 and type 2 sources in Figures 9–12. This plot shows the size–eccentricity trend (as it is seen in Figure 9) is not biased by the redshifts of the sources. Different morphological parameters of segmented regions in FRI and FRII galaxies are listed in Tables 1 and 2, respectively, for both the FIRST (italic) and LoTSS (bold) data sets. We aim to employ all these properties to define symmetry for radio galaxies in the following subsection.

4.3. Parameterizing Symmetry in Radio Galaxies

The definition that we present for symmetry is independent of the spatial orientation of the galaxy in the image. The only requirement is the matching of the center of the captured image with the optical center of the galaxy. Thus, to define symmetry parameters concerning the center of galaxies in the optical band, we need to discuss symmetry criteria based on the
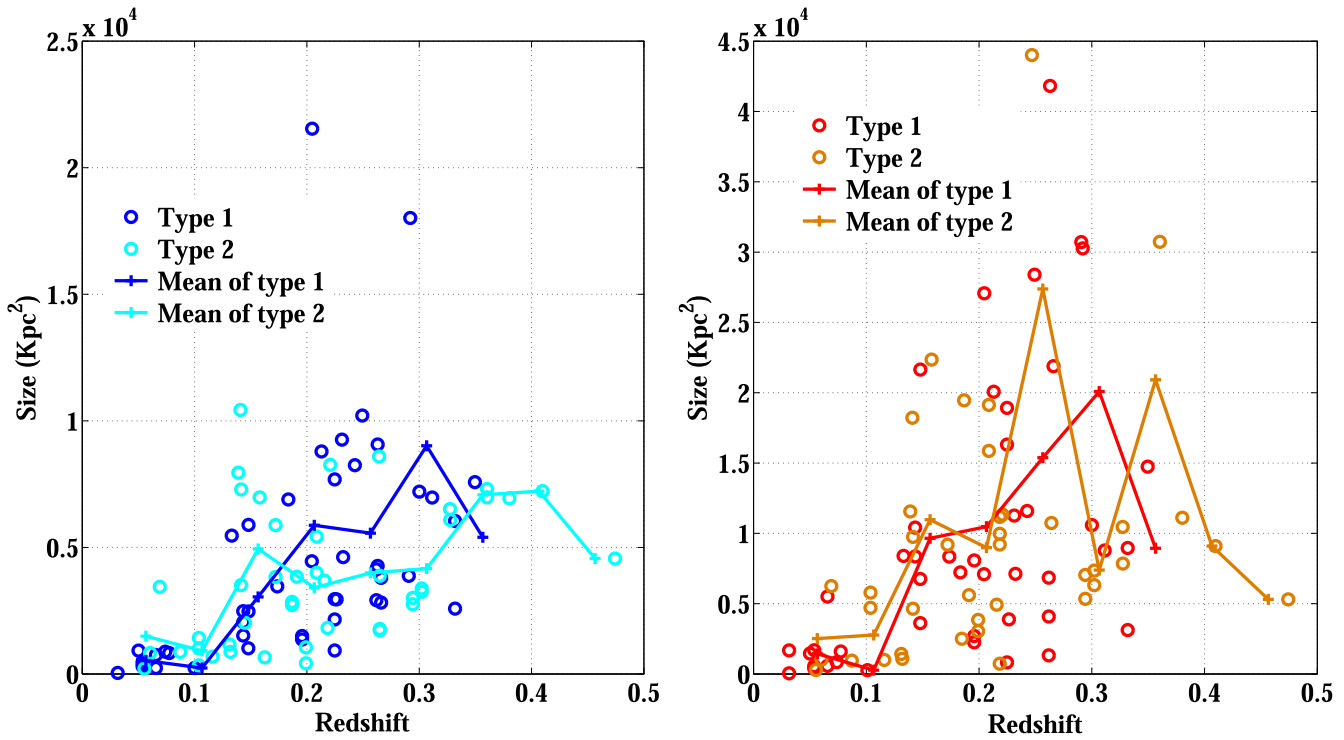
Figure 10. The relationship between the size of galaxies (kpc^2) and their redshift for mean values (shown by a +) of each bin (0.1, 0.2, etc.) for the FIRST and LoTSS data are demonstrated in the left and right scatter plots, respectively. The blue circles (with a whole mean of 4313 ± 64) and cyan circles (with a whole mean of 3806 ± 41) belong to type 1 and type 2 galaxies, respectively, in the FIRST data. The red circles (with a whole mean of 9735 ± 148) and orange circles (with a whole mean of 9259 ± 137) belong to type 1 and type 2 galaxies, respectively, in the LoTSS data.
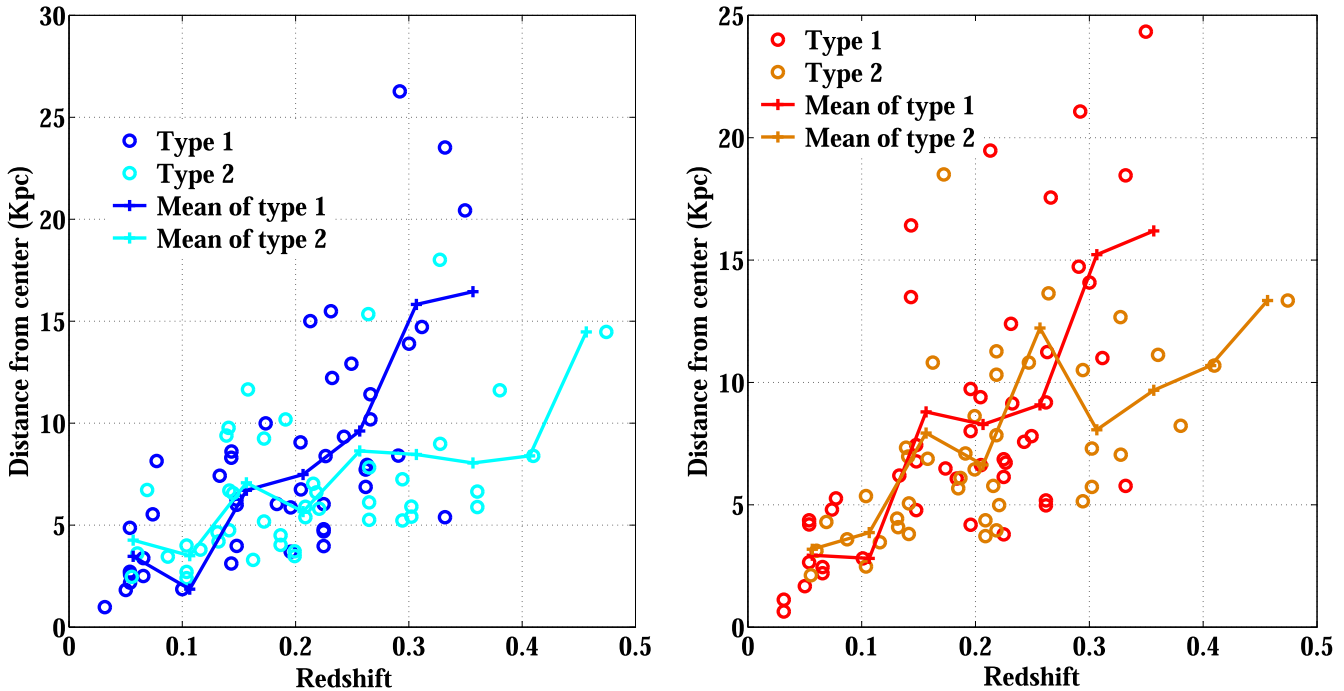
Figure 11. In these scatter plots, the distance from the centroid of the segmented region to the center of the image (center of the galaxy in the optical band) in terms of kiloparsec vs. redshift are presented for the FIRST and LoTSS data in the left and right scatter plots, respectively. As in the previous figures, the mean value of each bin (0.1, 0.2, etc.) is shown by a +. The blue circles (with a whole mean of 8.07 ± 0.08) and cyan circles (with a whole mean of 6.67 ± 0.05) belong to type 1 and type 2 galaxies, respectively, in the FIRST data. The red circles (with a whole mean of 8.34 ± 0.08) and orange circles (with a whole mean of 7.19 ± 0.06) belong to type 1 and type 2 galaxies, respectively, in the LoTSS data.

morphological properties of the extracted regions in galaxy maps. The code automatically gets the size of the image as input to find the quarter of the segmented region and the

distance between the intensity centroid of the region and the center of the image (the center of the galaxy in the optical band). For an image with one segmented region, the symmetry
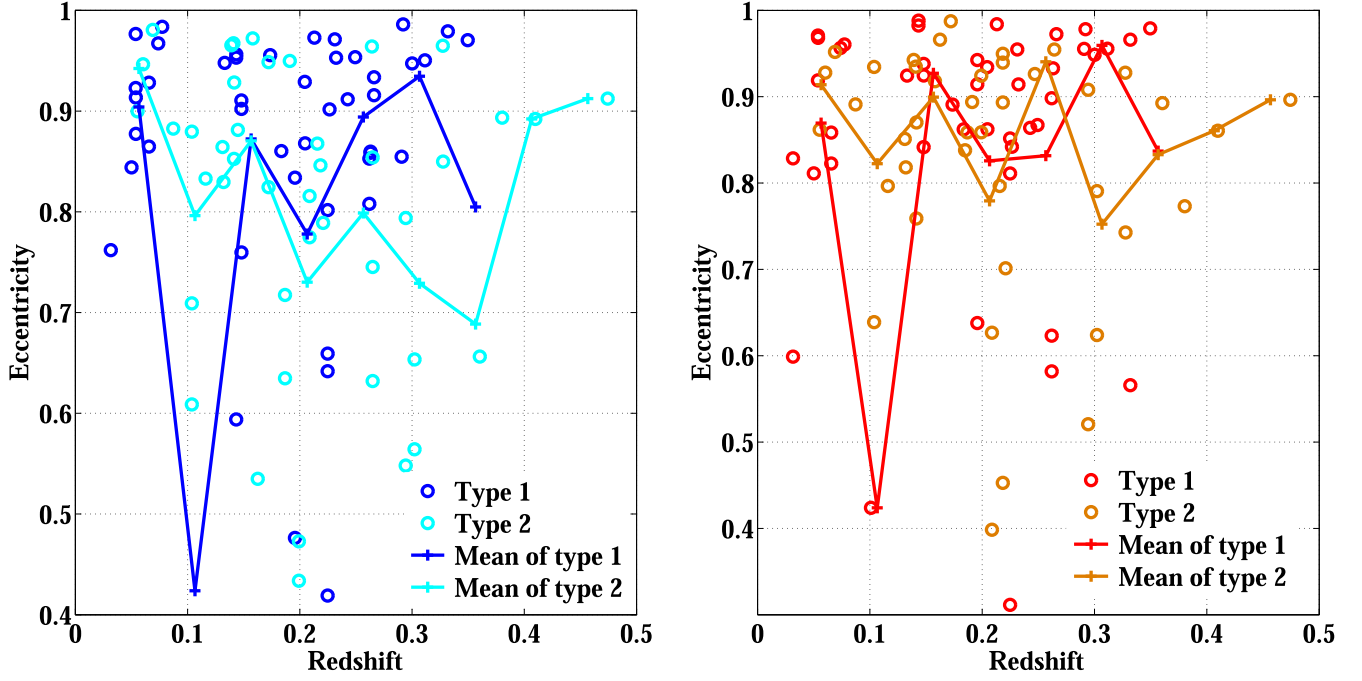
Figure 12. The relationship between the eccentricity of galaxies and their redshift for mean values (shown by a +) of each bin (0.1, 0.2, etc.) for the FIRST and LoTSS data are demonstrated in the left and right scatter plots, respectively. The blue circles (with a whole mean of 0.84 ± 0.02) and cyan circles (with a whole mean of 0.80 ± 0.02) belong to type 1 and type 2 galaxies, respectively, in the FIRST data. The red circles (with a whole mean of 0.86 ± 0.02) and orange circles (with a whole mean of 0.83 ± 0.02) belong to type 1 and type 2 galaxies, respectively, in the LoTSS data.
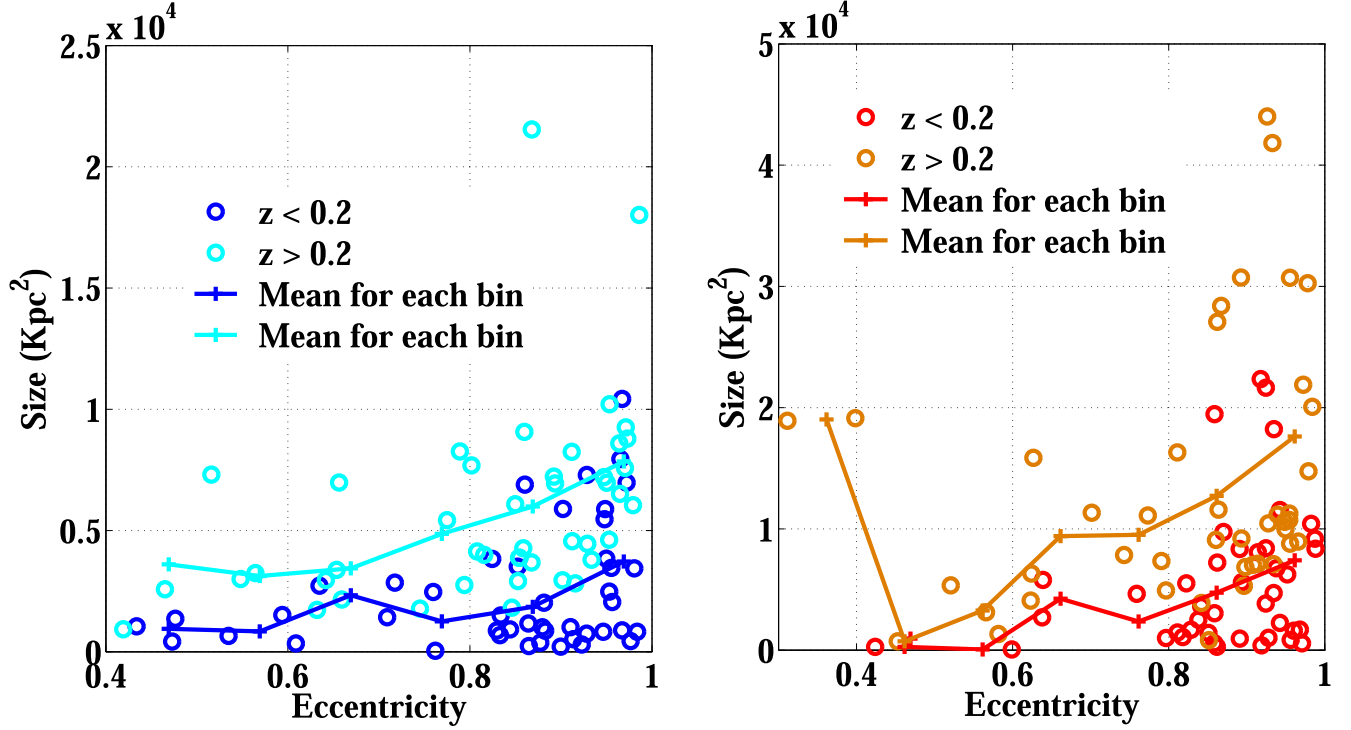
Figure 13. The relationship between the size of galaxies (kpc^2) and the eccentricity of galaxies for mean values (shown by a +) of each bin (0.1, 0.2, etc.) for the FIRST and LoTSS data are demonstrated in the left and right scatter plots, respectively. The blue circles (with a whole mean of 2438 ± 37) and cyan circles (with a whole mean of 5783 ± 58) belong to groups of galaxies with redshifts <0.2 and >0.2, respectively, in the FIRST data. The red circles (with a whole mean of 5597 ± 90) and orange circles (with a whole mean of $13,334 \pm 160$) belong to groups of galaxies with redshifts <0.2 and >0.2, respectively, in the LoTSS data.

of region $\mathcal{S}$ is obtained by multiplying two symmetries related to the proximity of the region centroid to the center of the image ($\mathcal{S}_{\text{proximity}}$) and eccentricity of the region ($\mathcal{S}_{\text{eccentricity}}$). For an image with more than one segmented region, in addition to the previous symmetries (with a slight difference in the

definition of the symmetry of proximity), two symmetries related to the quarters ($\mathcal{S}_{\text{quarter}}$) and orientations ($\mathcal{S}_{\text{orientation}}$) of the segmented regions are also defined. The range of all symmetries is [0, 1]. Symmetries with values of one and zero indicate the highest and lowest symmetry of the region,

Table 1
Main Components of the Segmented Regions in the FIRST (Italics) and LoTSS (Bold) Data Sets for FRI Galaxies

ID	Plate Julian Fiber	z	L-rad (W Hz^{-1})	Image size (rad) (pixels)	NoS	A[a]	$(X_{\mathrm{IWS}}, Y_{\mathrm{IWS}})$[a]	Q	$\lvert R - \odot\rvert$[a]	ε	Orientation (°)
1	886	0.0538	24.3	97.73		*124*	*(74, 91)*	*2*	*12.10*	*0.98 ± 0.01*	*−37.914 ± 0.003*
	52,381			*167²*	*2*	*84*	*(100, 70)*	*4*	*21.32*	*0.92 ± 0.02*	*−42.64 ± 0.04*
	523			**203²**	**2**	**227**	**(90, 111)**	**2**	**14.91**	**0.97 ± 0.01**	**−37.870 ± 0.002**
						159	**(123, 85)**	**4**	**27.10**	**0.92 ± 0.02**	**−38.90 ± 0.02**
2	907	0.0739	24.83	250.34							
	52,373			*167²*	*1*	*138*	*(82, 88)*	*2*	*4.74*	*0.97 ± 0.01*	*21.16 ± 0.02*
	231			**207²**	**1**	**190**	**(101, 106)**	**1**	**3.53**	**0.96 ± 0.01**	**21.99 ± 0.01**
3	1014	0.148	24.85	75.33		*272*	*(79, 75)*	*3*	**9.62**	*0.90 ± 0.01*	*44.213 ± 0.003*
	52,707			*167²*	*2*	*114*	*(104, 100)*	*1*	*26.31*	*0.76 ± 0.06*	*2.59 ± 0.05*
	5			**207²**	**1**	**1440**	**(109, 104)**	**1**	**7.10**	**0.925 ± 0.005**	**39.610 ± 0.002**
4	1048	0.2044	24.94	29.16							
	52,736			*167²*	*1*	*122*	*(83, 83)*	*3*	*0.70*	*0.93 ± 0.02*	*−43.96 ± 0.03*
	588			**207²**	**1**	**280**	**(103, 101)**	**3**	**2.54**	**0.93 ± 0.01**	**42.15 ± 0.01**
5	1164	0.1331	24.91	64.2							
	52,674			*167²*	*1*	*302*	*(86, 82)*	*4*	*2.91*	*0.95 ± 0.01*	*−30.67 ± 0.01*
	103			**209²**	**1**	**668**	**(109, 105)**	**1**	**4.52**	**0.92 ± 0.01**	**−36.677 ± 0.003**
6	1165	0.2661	25.06	57.4		*52*	*(79, 76)*	*3*	*8.74*	*0.92 ± 0.03*	*−30.79 ± 0.01*
	52,703			*167²*	*2*	*70*	*(88, 91)*	*1*	*8.74*	*0.93 ± 0.02*	*−33.06 ± 0.04*
	468			**204²**	**1**	**581**	**(101, 102)**	**3**	**1**	**0.972 ± 0.003**	**−40.490 ± 0.003**
7	1279	0.3496	25.42	36.15							
	52,736			*167²*	*1*	*96*	*(84, 84)*	*1*	*0.70*	*0.97 ± 0.01*	*38.40 ± 0.02*
	476			**204²**	**1**	**269**	**(103, 101)**	**4**	**1.41**	**0.98 ± 0.01**	**36.26 ± 0.01**
8	1310	0.0501	23.43	42.73							
	53,033			*167²*	*1*	*298*	*(83, 84)*	*2*	*0.70*	*0.84 ± 0.02*	*−35.55 ± 0.01*
	203			**204²**	**1**	**674**	**(103, 106)**	**1**	**4.12**	**0.81 ± 0.02**	**36.44 ± 0.01**
9	1315	0.2047	25.02	52.27							
	52,791			*167²*	*1*	*589*	*(84, 83)*	*4*	*0.70*	*0.87 ± 0.01*	*14.98 ± 0.06*
	1			**205²**	**1**	**1066**	**(104, 102)**	**4**	**1.58**	**0.86 ± 0.01**	**14.793 ± 0.004**
10	1322	0.1434	24.47	29.55							
	52,791			*167²*	*1*	*100*	*(83, 84)*	*2*	*0.70*	*0.96 ± 0.01*	*−1.84 ± 0.02*
	27			**207²**	**1**	**586**	**(103, 105)**	**2**	**1.58**	**0.99 ± 0.002**	**13.614 ± 0.002**
11	1327	0.292	25.31	67.26							
	52,781			*167²*	*1*	*291*	*(83, 84)*	*2*	*0.70*	*0.9861 ± 0.0029*	*32.2458 ± 0.0051*
	358			**206²**	**1**	**704**	**(101, 105)**	**2**	**2.82**	**0.978 ± 0.003**	**38.535 ± 0.002**
12	1328	0.1736	25.15	51.63							
	52,786			*167²*	*1*	*123*	*(84, 83)*	*4*	*0.70*	*0.96 ± 0.01*	*10.1568 ± 0.02*
	309			**206²**	**1**	**427**	**(104, 102)**	**4**	**1.41**	**0.89 ± 0.01**	**28.94 ± 0.01**
13	1369	0.0213	25.08	72.27							
	53,089			*167²*	*1*	*226*	*(81, 84)*	*2*	*2.54*	*0.97 ± 0.01*	*−16.93 ± 0.01*
	588			**203²**	**1**	**743**	**(96, 100)**	**3**	**5.70**	**0.984 ± 0.002**	**−16.726 ± 0.002**
14	1449	0.0656	24.43	57.47		*146*	*(90, 83)*	*4*	*6.52*	*0.93 ± 0.02*	*−2.17 ± 0.01*
	53,116			*167²*	*2*	*46*	*(90, 96)*	*1*	*14.09*	*0.87 ± 0.05*	*5.76 ± 0.08*
	419			**203²**	**2**	**1544**	**(103, 101)**	**4**	**1.58**	**0.82 ± 0.01**	**2.752 ± 0.002**
						161	**(149, 103)**	**1**	**47.52**	**0.86 ± 0.03**	**−26.89 ± 0.02**
15	1465	0.2248	24.97	110.23		*182*	*(79, 62)*	*3*	*21.96*	*0.80 ± 0.03*	*−16.082 ± 0.002*
	53,082					*22*	*(84, 84)*	*1*	*0.70*	*0.42 ± 0.39*	*−18.409 ± 0.004*
	522					*51*	*(84, 97)*	*1*	*13.51*	*0.66 ± 0.12*	*−30.54 ± 0.01*
				167²	*4*	*70*	*(93, 113)*	*1*	*30.99*	*0.64 ± 0.11*	*16.79 ± 0.32*
				204²	**3**	**645**	**(96, 74)**	**3**	**28.63**	**0.31 ± 0.10**	**−13.62 ± 0.01**
						556	**(106, 128)**	**1**	**26.30**	**0.81 ± 0.02**	**−7.31 ± 0.01**
						28	**(102, 100)**	**3**	**2**	**0.85 ± 0.07**	**−6.70 ± 0.15**
16	1671	0.0774	24.16	38.67							
	53,446			*167²*	*1*	*119*	*(83, 83)*	*3*	*0.70*	*0.98 ± 0.01*	*−26.99 ± 0.01*

Table 1
(Continued)

ID	Plate Julian Fiber	z	L-rad (W Hz^{-1})	Image size (rad) (*pixels*)	NoS	A[a]	$(X_\mathrm{IWS}, Y_\mathrm{IWS})$[a]	Q	$\lvert R - \odot \rvert$[a]	ε	Orientation (°)
	603			**208^2**	**1**	**331**	**(104, 103)**	**3**	**1**	**0.96 ± 0.01**	**−30.68 ± 0.01**
17	967 52,636 312	0.0316	24.22	126.8 *167^2* **205^2**	*1* **2**	*33* **1873** 57	*(84, 84)* **(127, 109)** (104, 62)	*1* **1** 4	*0.70* **25.34** 40.52	*0.76 ± 0.10* **0.83 ± 0.01** **0.60 ± 0.19**	*5.62 ± 0.24* **−25.854 ± 0.003** **−42.75 ± 0.34**
18	1278 52,735 558	0.1479	24.76	94.15 *167^2* **206^2**	*1* **2**	*47* **450** 241	*(84, 84)* **(94, 110)** (103, 74)	*1* **2** 3	*0.70* **11.40** 29	*0.91 ± 0.04* **0.94 ± 0.01** **0.84 ± 0.02**	*7.63 ± 0.07* **15.554 ± 0.002** **−0.42 ± 0.02**
19	1279 52,736 479	0.2493	25.56	84.32 *167^2* **204^2**	*1* **1**	*207* **829**	*(85, 86)* **(105, 109)**	*1* **1**	*2.91* **7.61**	*0.95 ± 0.01* **0.87 ± 0.01**	*37.12 ± 0.01* **42.784 ± 0.004**
20	1672 53,460 394	0.1835	24.75	35.34 *167^2* **204^2**	*1* **1**	*224* **338**	*(78, 88)* **(97, 110)**	*2* **2**	*7.11* **9.21**	*0.86 ± 0.02* **0.86 ± 0.02**	*1.49 ± 0.02* **0.75 ± 0.01**
21	883 52,430 616	0.1957	25.03	37.6 *167^2* **205^2**	*2* **3**	*44* *40* **341** 114 95	*(76, 81)* *(90, 89)* **(89, 106)** (110, 109) (127, 124)	*3* *1* **2** 1 1	*7.90* *8.51* **13.94** 9.92 32.59	*0.83 ± 0.07* *0.48 ± 0.24* **0.91 ± 0.01** **0.64 ± 0.087** **0.94 ± 0.02**	*31.71 ± 0.01* *−23.82 ± 0.24* **25.614 ± 0.002** **40.928 ± 0.004** **33.37 ± 0.02**
22	965 52,438 362	0.3115	25.8	34.46 *167^2* **207^2**	*1* **1**	*103* **371**	*(85, 83)* **(106, 103)**	*4* **4**	*1.58* **2.54**	*0.95 ± 0.01* **0.96 ± 0.01**	*43.64 ± 0.02* **−43.60 ± 0.01**
23	966 52,642 604	0.0539	23.45	61.15 *167^2* **204^2**	*2* **1**	*145* *104* **684**	*(74, 72)* *(92, 96)* **(101, 98)**	*3* *1* **3**	*14.92* *15.12* **4.12**	*0.91 ± 0.02* *0.88 ± 0.03* **0.968 ± 0.003**	*−36.646 ± 0.003* *37.59 ± 0.03* **−38.842 ± 0.002**
24	971 52,644 205	0.2619	24.9	61.54 *167^2* **206^2**	*2* **3**	*78* *55* **186** 36 111	*(71, 83)* *(104, 77)* **(88, 102)** (108, 62) (128, 95)	*3* *4* **3** 4 4	*12.51* *21.51* **15.03** 41.30 26.24	*0.81 ± 0.06* *0.85 ± 0.05* **0.90 ± 0.018** **0.58 ± 0.18** **0.62 ± 0.09**	*−8.488 ± 0.004* *−29.24 ± 0.62* **−8.648 ± 0.002** **−30.511 ± 0.003** **−0.68 ± 0.07**
25	1014 52,707 221	0.2312	25.08	37.82 *167^2* **205^2**	*1* **1**	*210* **368**	*(84, 83)* **(103, 102)**	*4* **4**	*0.70* **0.70**	*0.97 ± 0.01* **0.96 ± 0.01**	*8.95 ± 0.01* **9.74 ± 0.01**
26	1017 52,706 182	0.1433	24.48	57.9 *167^2* **203^2**	*2* **1**	*121* *74* **731**	*(75, 80)* *(98, 86)* **(100, 100)**	*3* *1* **3**	*19.19* *14.71* **2.12**	*0.95 ± 0.01* *0.59 ± 0.12* **0.983 ± 0.002**	*14.84 ± 0.01* *35.25 ± 0.12* **17.463 ± 0.002**
27	1041 52,724 87	0.3319	25.33	30.61 *167^2* **204^2**	*2* **2**	*35* *82* **61** 175	*(70, 71)* *(84, 83)* **(85, 87)** (103, 101)	*3* *4* **3** 4	*18.40* *0.70* **22.67** 1.41	*0.47 ± 0.27* *0.98 ± 0.01* **0.57 ± 0.15** **0.97 ± 0.01**	*41.30 ± 0.01* *20.31 ± 0.02* **40.304 ± 0.004** **17.02 ± 0.01**
28	1044 52,468 220	0.2630	25.13	47.75 *167^2* **203^2**	*2* **1**	*170* *80* **1129**	*(81, 79)* *(85, 97)* **(98, 103)**	*3* *1* **2**	*5.15* *13.58* **3.80**	*0.86 ± 0.02* *0.86 ± 0.04* **0.93 ± 0.01**	*−13.10 ± 0.01* *40.49 ± 0.05* **41.80 ± 0.002**
29	1161 52,703 145	0.2907	25.0	67.72 *167^2* **207^2**	*1* **1**	*63* **719**	*(68, 89)* **(102, 113)**	*2* **2**	*16.45* **9.61**	*0.86 ± 0.05* **0.96 ± 0.004**	*−15.31 ± 0.06* **6.52 ± 0.002**
30	1165 52,703 524	0.3001	25.03	24.47 *167^2* **203^2**	*1* **1**	*112* **237**	*(86, 84)* **(101, 101)**	*1* **3**	*2.55* **0.70**	*0.95 ± 0.02* **0.95 ± 0.01**	*33.66 ± 0.02* **35.58 ± 0.01**
31	1282 52,759 237	0.2323	25.0	18.02 *167^2* **203^2**	*1* **1**	*104* **231**	*(85, 84)* **(104, 101)**	*1* **4**	*1.58* **2.54**	*0.95 ± 0.01* **0.91 ± 0.02**	*44.23 ± 0.02* **−44.17 ± 0.01**

Table 1
(Continued)

ID	Plate Julian Fiber	z	L-rad (W Hz^{-1})	Image size (rad) (*pixels*)	NoS	A^{a}	$(X_{\text{IWS}}, Y_{\text{IWS}})^{\text{a}}$	Q	$|R - \odot|^{\text{a}}$	ε	Orientation (°)
32	1310	0.2265	24.91	15.06							
	53,033			*167*^{2}	*1*	*69*	*(84, 83)*	*4*	*0.70*	*0.90 ± 0.03*	*−4.68 ± 0.05*
	282			**207**^{2}	**1**	**131**	**(105, 104)**	**1**	**1.58**	**0.84 ± 0.04**	**−3.28 ± 0.03**
33	1449	0.1010	24.65	202.19							
	53,116			*167*^{2}	*1*	*21*	*(83, 83)*	*3*	*0.70*	*0.3333 ± 0.0001*	*−40.70 ± 0.27*
	53			**206**^{2}	**1**	**35**	**(103, 103)**	**0**	**0**	**0.42 ± 0.32**	**−35.05 ± 0.41**
34	1466	0.2427	25.16	28.53							
	53,083			*167*^{2}	*1*	*174*	*(82, 83)*	*3*	*1.58*	*0.91 ± 0.02*	*6.14 ± 0.02*
	507			**205**^{2}	**1**	**352**	**(102, 101)**	**3**	**1.58**	**0.86 ± 0.02**	**7.20 ± 0.01**

Note. The first column is the radio galaxy ID. Plate, Julian, Fiber are the unique ID of the galaxy in the the SDSS catalog. z presents the redshift of the galaxy. L-rad is the logarithm of the total radio luminosity of the galaxy in the unit of W Hz^{-1}. NoS, A, and Q are the abbreviations of "Number of Segments," "Area," and "Quarter," respectively.

[a] The unit of the column is in terms of the pixel. $|R - \odot|$ is the magnitude value of the distance between the IWC of the segmented region and origin. Also, the origin is the center of the galaxy in the optical band that corresponds to the center of the image.

respectively. The multiplication of symmetries provides a final symmetry value related to the case of interest, which also ranges from [0, 1]. Four different cases correspond to the number of the segregated regions as counted in each map are described below in detail.

Case I: this corresponds to the radio maps with only one segmented region. Therefore, we deal with a segmented region in an image close to or away from the center (see the circle-like segments in the left-side image of Figure 14). We define the first parameter of symmetry based on the proximity of the IWC of a region to the center of the image (i.e., the center of the galaxy in the optical band). We assigned a value of one for proximity measure $\mathcal{S}_{\text{proximity}}$ if the centroid of the region is placed in the center of the image, and a value of zero is assigned when the position of the centroid is at the end of the radius of the circle which is noted in Section 3.2.

Since circle-like shapes are more symmetrical than elongated shapes, we define the second measure of symmetry related to the eccentricity parameter. Since a circle (with $\varepsilon = 0$) has more symmetry than any type of elliptical shape, we define an eccentricity-based symmetry. Any shape mapped to a circle takes the highest symmetry value (i.e., $\mathcal{S}_{\text{eccentricity}} = 1$), and any elongated shape like a line (with $\varepsilon = 1$) takes the lowest symmetry value (i.e., $\mathcal{S}_{\text{eccentricity}} = 0$). So, using Equation (7), the relation $\frac{1 - \varepsilon}{1}$ gives the value of $\mathcal{S}_{\text{eccentricity}}$ for any segmented region. In other words, we assigned a value of one for the eccentricity measure $\mathcal{S}_{\text{eccentricity}}$ if the eccentricity of the shape returns a value of zero (circle), and a value of zero for $\mathcal{S}_{\text{eccentricity}}$ belongs to shapes with eccentricities of 1 (line). The value of $\mathcal{S}_{\text{eccentricity}}$ for any type of shape ranges from [0, 1]. Thus, the multiplication of these parameters as $\mathcal{S}_{\text{proximity}} \times \mathcal{S}_{\text{eccentricity}}$ gives a symmetry criterion $\mathcal{S}$ in the range of zero (completely asymmetric) and one (perfectly symmetric). For more explanations, see the caption of Figure 14. As an example, the distance of the IWC of a segmented radio galaxy with ID number 43 (see Table 2) to the center of the image in the LoTSS data is one pixel (1″5) and the size of the image is 202^2 pixels. The distance from the center of the image to the end of the area of interest is 101 pixels (151″5). Thus, $\mathcal{S}_{\text{proximity}}$ equals 0.99 (i.e., $|\frac{101 - 1}{101}|$ or $|\frac{151.5 - 1.5}{151.5}|$).

Moreover, the eccentricity of the object is about 0.8, which leads to the value of 0.2 (i.e., $\frac{1 - 0.8}{1}$) for $\mathcal{S}_{\text{eccentricity}}$. Therefore, the multiplication of these parameters gives the symmetry criterion $\mathcal{S} = 0.2$.

Case II: this corresponds to radio maps with two segmented regions (Figure 14, two right-side configurations). At first, the two-dimensional image is divided into four equal quarters using the x- and y-axes so that the respective coordinate axes intersect each other in the optical center (center of image). The first parameter that must be considered in defining the symmetry for two regions is the quarters (q', q'') of the IWCs $\mathcal{S}_{\text{quarter}}$ (see Figure 15 and its caption for the definition of quarters). The centroids of the two segmented regions must be in quarters wherein $|q' - q''| = 2$. In other words, if the centroids are in quarters 1 and 3 or in quarters 2 and 4, then $\mathcal{S}_{\text{quarter}} = 1$; otherwise, $\mathcal{S}_{\text{quarter}} = 0$ (Figure 14, configurations 1 and 2). The other parameter is the proximity of the centroids to the center of the image. We updated the definition of $\mathcal{S}_{\text{proximity}}$ in Case I to illustrate the symmetry for two segmented sources. In this case, when the centroids are equidistant from the center of the image, $\mathcal{S}_{\text{proximity}} = 1$ (orange and blue dashed lines in Figure 14). If they are farthest apart, one at the point closest to the center and the other at the farthest point from the center, then $\mathcal{S}_{\text{proximity}} = 0$. In fact, to obtain $\mathcal{S}_{\text{proximity}}$, we compute the relation $\frac{\text{radius of the circle (half image side)} - |D_{q'} - D_{q''}|}{\text{radius of the circle (half image side)}}$, wherein $D_{q'}$ and $D_{q''}$ are the magnitude values of the distances of the centroids from the center of image, which appear in quarters q' and q'', respectively. The third and fourth parameters are related to the similarity of regions expressed by eccentricity and orientation. Here, if the regions in two quarters have the same eccentricities, $\mathcal{S}_{\text{eccentricity}} = 1$. If the value of the difference between eccentricities is a maximum (i.e., $1 - 0 = 1$) for the two regions, then $\mathcal{S}_{\text{eccentricity}} = 0$. Therefore, for finding $\mathcal{S}_{\text{eccentricity}}$, we compute the simple relation $\frac{1 - |\varepsilon_{q'} - \varepsilon_{q''}|}{1}$, wherein $\varepsilon_{q'}$ and $\varepsilon_{q''}$ are the eccentricities of the regions in quarters q' and q'', respectively. By exploiting the formulas presented in Section 3.3, the direction of the segmented region is determined relative to the positive x-axis (the angle ω between the major axis of a shape and the horizontal x-axis that passes through the

Table 2
Main Components of the Segmented Regions in the FIRST (Italics) and LoTSS (Bold) Data Sets for the FRII Galaxies

ID	Plate Julian Fiber	z	L-rad (W Hz^{-1})	Image size (rad) (pixels)	NoS	$A^\star$	$(X_{\mathrm{IWS}}, Y_{\mathrm{IWS}})^\star$	Q	$\lvert R - \odot \rvert^\star$	ε	Orientation (°)
35	881 52,368 501	0.3803	25.35	12.68 *167²* **209²**	*1* **1**	*79* **182**	*(83, 84)* **(103, 104)**	*2* **3**	*0.70* **1.58**	*0.89 ± 0.03* **0.77 ± 0.04**	*3.51 ± 0.04* **5.71 ± 0.03**
36	885 52,379 168	0.2208	24.88	22.52 *167²* **203²**	*1* **1**	*201* **397**	*(83, 82)* **(101, 99)**	*3* **3**	*1.58* **2.54**	*0.79 ± 0.04* **0.70 ± 0.04**	*−17.95 ± 0.02* **−12.43 ± 0.02**
37	907 52,373 461	0.3604	25.27	35.49 *167²* **206²**	*2* **1**	*89* *85* **539**	*(81, 94)* *(91, 77)* **(106, 106)**	*2* *4* **1**	*10.79* *9.92* **4.24**	*0.52 ± 0.14* *0.66 ± 0.10* **0.89 ± 0.01**	*32.29 ± 0.01* *−16.18 ± 0.10* **25.16 ± 0.01**
38	963 52,643 505	0.4743	26.05	9.99 *167²* **205²**	*1* **1**	*40* **67**	*(84, 82)* **(102, 101)**	*4* **3**	*1.58* **1.58**	*0.91 ± 0.04* **0.90 ± 0.04**	*19.19 ± 0.07* **19.86 ± 0.05**
39	969 52,442 491	0.2087	24.9	104.62 *167²* **209²**	*2* **2**	*144* *106* **731** **606**	*(64, 68)* *(106, 105)* **(85, 86)** **(129, 125)**	*3* *1* **3** **1**	*24.91* *31.12* **26.87** **31.94**	*0.78 ± 0.05* *0.82 ± 0.04* **0.40 ± 0.07** **0.63 ± 0.04**	*41.105 ± 0.002* *33.71 ± 0.04* **41.611 ± 0.001** **29.17 ± 0.01**
40	969 52,442 530	0.1848	24.79	10.82 *167²* **205²**	*1* **1**	*65* **116**	*(83, 84)* **(102, 103)**	*2* **2**	*0.70* **0.70**	*0.88 ± 0.04* **0.84 ± 0.04**	*4.44 ± 0.05* **2.47 ± 0.04**
41	970 52,413 287	0.2943	25.5	24.53 *167²* **203²**	*2* **1**	*48* *44* **285**	*(79, 90)* *(87, 80)* **(101, 105)**	*2* *4* **2**	*7.91* *4.95* **6.09**	*0.55 ± 0.18* *0.79 ± 0.08* **0.71 ± 0.07**	*41.65 ± 0.01* *−21.60 ± 0.16* **−31.38 ± 0.01**
42	970 52,413 543	0.1992	25.82	196.39 *167²* **207²**	*2* **2**	*12* *30* **158** **125**	*(39, 94)* *(144, 66)* **(55, 114)** **(174, 81)**	*2* *4* **2** **4**	*45.72* *62.98* **49.62** **47.00**	*0.47 ± 0.43* *0.43 ± 0.34* **0.92 ± 0.02** **0.86 ± 0.03**	*−14.741 ± 0.002* *12.19 ± 0.51* **−15.065 ± 0.001** **44.09 ± 0.04**
43	1012 52,649 197	0.2156	25.12	12.02 *167²* **202²**	*1* **1**	*93* **179**	*(84, 83)* **(102, 100)**	*4* **4**	*0.70* **1**	*0.87 ± 0.04* **0.80 ± 0.04**	*−34.30 ± 0.04* **−33.32 ± 0.03**
44	1013 52,707 165	0.1038	24.34	103.19 *167²* **206²**	*3* **2**	*86* *29* *121* **576** **708**	*(61, 78)* *(83, 84)* *(116, 97)* **(79, 100)** **(142, 119)**	*3* *2* *1* **3** **1**	*23.16* *0.70* *35.19* **24.18** **42.15**	*0.88 ± 0.05* *0.61 ± 0.19* *0.71 ± 0.07* **0.935 ± 0.006** **0.64 ± 0.03**	*19.790 ± 0.002* *22.630 ± 0.003* *−33.39 ± 0.07* **16.683 ± 0.001** **−12.76 ± 0.01**
45	1015 52,734 478	0.0554	23.48	9.89 *167²* **205²**	*1* **1**	*57* **108**	*(84, 83)* **(102, 102)**	*4* **3**	*0.70* **0.70**	*0.90 ± 0.04* **0.86 ± 0.04**	*10.46 ± 0.06* **10.90 ± 0.04**
46	1017 52,706 284	0.0603	23.8	31.28 *167²* **204²**	*1* **1**	*188* **334**	*(83, 84)* **(102, 102)**	*2* **0**	*0.70* **0**	*0.95 ± 0.01* **0.93 ± 0.01**	*−5.06 ± 0.01* **−4.55 ± 0.01**
47	1042 52,725 519	0.1409	25.76	79.28 *167²* **203²**	*1* **1**	*523* **1316**	*(88, 85)* **(107, 103)**	*1* **1**	*4.74* **5.70**	*0.97 ± 0.004* **0.94 ± 0.01**	*34.408 ± 0.004* **33.732 ± 0.002**
48	1042 52,725 594	0.1625	25.36	287.95 *167²* **207²**	*1* **1**	*26* **10,237**	*(84, 93)* **(99, 104)**	*4* **2**	*0.70* **4.52**	*0.54 ± 0.25* **0.966 ± 0.001**	*−4.04 ± 0.48* **−40.1370 ± 0.0002**
49	1043 52,465 100	0.132	24.6	8.03 *167²* **208²**	*1* **1**	*49* **87**	*(83, 83)* **(104, 103)**	*3* **3**	*0.70* **1**	*0.83 ± 0.06* **0.82 ± 0.05**	*7.27 ± 0.09* **−1.57 ± 0.06**
50	1046 52,460 233	0.1911	24.74	19.82 *167²* **209²**	*1* **1**	*117* **246**	*(83, 83)* **(104, 104)**	*3* **3**	*0.70* **0.70**	*0.95 ± 0.01* **0.89 ± 0.02**	*−32.51 ± 0.02* **−30.44 ± 0.01**

Table 2
(Continued)

ID	Plate Julian Fiber	z	L-rad (W Hz^{-1})	Image size (rad) (pix**els**)	NoS	A*	$(X_{\text{IWS}}, Y_{\text{IWS}})^\star$	Q	$\lvert R-\odot\rvert^\star$	ε	Orientation (°)
51	1049	0.0872	24.59	13.16							
	52,751			167^2	*1*	*101*	*(83, 84)*	*2*	*0.70*	*0.88 ± 0.03*	*−6.13 ± 0.03*
	381			**209^2**	**1**	**158**	**(104, 104)**	**3**	**0.70**	**0.89 ± 0.02**	**−9.22 ± 0.02**
52	1282	0.3276	25.32	11.0							
	52,759			167^2	*1*	*84*	*(83, 84)*	*2*	*0.70*	*0.85 ± 0.04*	*24.75 ± 0.05*
	19			**204^2**	**1**	**156**	**(101, 101)**	**3**	**1.41**	**0.74 ± 0.05**	**−25.18 ± 0.04**
53	1283	0.3022	25.1	26.94		*52*	*(81, 76)*	*3*	*7.90*	*0.65 ± 0.12*	*−24.87 ± 0.01*
	52,762			167^2	*2*	*50*	*(87, 90)*	*1*	*7.38*	*0.56 ± 0.17*	*−27.42 ± 0.22*
	178			**207^2**	**2**	**163**	**(102, 95)**	**3**	**8.63**	**0.79 ± 0.04**	**−20.59 ± 0.01**
						140	**(108, 111)**	**1**	**8.74**	**0.62 ± 0.08**	**−6.32 ± 0.08**
54	1314	0.4098	25.47	13.35							
	53,050			167^2	*1*	*75*	*(84, 84)*	*1*	*0.70*	*0.89 ± 0.03*	*−17.38 ± 0.05*
	84			**203^2**	**1**	**136**	**(102, 102)**	**1**	**0.70**	**0.86 ± 0.03**	**−18.79 ± 0.03**
55	1444	0.1160	25.46	7.93							
	53,054			167^2	*1*	*48*	*(83, 84)*	*2*	*0.70*	*0.83 ± 0.06*	*37.18 ± 0.10*
	96			**205^2**	**1**	**101**	**(102, 102)**	**3**	**0.70**	**0.80 ± 0.05**	**37.68 ± 0.06**
56	1455	0.1415	24.84	43.04							
	53,089			167^2	*1*	*363*	*(84, 84)*	*1*	*0.70*	*0.93 ± 0.01*	*−21.69 ± 0.01*
	236			**204^2**	**1**	**699**	**(101, 103)**	**2**	**1.41**	**0.87 ± 0.01**	**−21.54 ± 0.01**
57	1459	0.2184	25.38	8.26							
	53,117			167^2	*1*	*45*	*(84, 84)*	*1*	*0.70*	*0.85 ± 0.06*	*36.86 ± 0.08*
	173			**206^2**	**4**	**328**	**(64, 126)**	**2**	**45.27**	**0.89 ± 0.02**	**8.341 ± 0.001**
						26	**(74, 104)**	**2**	**29.01**	**0.45 ± 0.32**	**30.092 ± 0.001**
						355	**(100, 105)**	**2**	**3.60**	**0.95 ± 0.01**	**−42.884 ± 0.001**
						398	**(128, 134)**	**1**	**39.82**	**0.94 ± 0.01**	**−28.34 ± 0.01**
58	1675	0.1311	24.77	10.05							
	53,466			167^2	*1*	*66*	*(83, 84)*	*2*	*0.70*	*0.86 ± 0.05*	*3.15 ± 0.06*
	619			**207^2**	**1**	**116**	**(103, 104)**	**2**	**0.70**	**0.85 ± 0.04**	**2.31 ± 0.04**
59	793	0.1580	24.77	51.56							
	52,370			167^2	*1*	*289*	*(83, 83)*	*3*	*0.70*	*0.972 ± 0.004*	*−17.30 ± 0.01*
	12			**205^2**	**1**	**1334**	**(102, 101)**	**3**	**1.58**	**0.92 ± 0.01**	**−28.080 ± 0.002**
60	908	0.1390	24.35	59.85							
	52,373			167^2	*1*	*408*	*(83, 83)*	*3*	*0.70*	*0.97 ± 0.01*	*−21.460 ± 0.004*
	56			**206^2**	**1**	**854**	**(102, 101)**	**3**	**2.23**	**0.94 ± 0.01**	**−17.852 ± 0.003**
61	971	0.2649	24.93	68.58		*72*	*(73, 96)*	*2*	*16.32*	*0.85 ± 0.04*	*44.96 ± 0.01*
	52,644					*33*	*(84, 83)*	*4*	*0.70*	*0.75 ± 0.11*	*−40.67 ± 0.01*
	150			167^2	*3*	*32*	*(98, 70)*	*4*	*19.81*	*0.63 ± 0.16*	*41.72 ± 0.48*
				204^2	**1**	**1176**	**(102, 103)**	**1**	**1**	**0.926 ± 0.006**	**−35.240 ± 0.002**
62	1010	0.1868	24.72	47.67		*86*	*(74, 86)*	*2*	*9.82*	*0.64 ± 0.10*	*−35.10 ± 0.01*
	52,649			167^2	*2*	*90*	*(94, 71)*	*4*	*16.32*	*0.72 ± 0.08*	*23.74 ± 0.12*
	199			**211^2**	**1**	**885**	**(106, 94)**	**4**	**11.51**	**0.86 ± 0.01**	**−36.290 ± 0.003**
63	1016	0.0690	24.16	97.53							
	52,759			167^2	*1*	*611*	*(86, 85)*	*1*	*2.91*	*0.980 ± 0.003*	*5.995 ± 0.002*
	293			**204^2**	**1**	**1598**	**(103, 103)**	**1**	**1.41**	**0.952 ± 0.004**	**4.395 ± 0.001**
64	1163	0.1414	24.74	22.61							
	52,669			167^2	*1*	*175*	*(83, 83)*	*3*	*0.70*	*0.85 ± 0.03*	*41.27 ± 0.02*
	170			**206^2**	**1**	**333**	**(102, 102)**	**3**	**1.41**	**0.76 ± 0.03**	**42.07 ± 0.02**
65	1284	0.1721	24.72	53.07		*212*	*(81, 96)*	*2*	*12.75*	*0.95 ± 0.01*	*14.942 ± 0.004*
	52,736			167^2	*2*	*138*	*(88, 68)*	*4*	*16.14*	*0.83 ± 0.03*	*7.14 ± 0.04*
	268			**205^2**	**1**	**477**	**(103, 106)**	**1**	**3.53**	**0.987 ± 0.002**	**11.848 ± 0.003**
66	1325	0.3274	25.23	24.03							
	52,762			167^2	*1*	*90*	*(83, 83)*	*3*	*0.70*	*0.97 ± 0.01*	*21.33 ± 0.02*
	337			**209^2**	**1**	**208**	**(105, 103)**	**4**	**1.58**	**0.93 ± 0.02**	**22.81 ± 0.01**

Table 2
(Continued)

ID	Plate Julian Fiber	z	L-rad (W Hz^{-1})	Image size (rad) (pixels)	NoS	A*	(X_{IWS}, Y_{IWS})*	Q	$\|R - \odot\|^\star$	ε	Orientation (°)
67	1442	0.2642	25.04	29.18							
	53,050			167^2	1	160	(83, 83)	3	0.70	0.96 ± 0.01	15.79 ± 0.01
	141			$\mathbf{205^2}$	**1**	**288**	**(101, 102)**	**3**	**1.58**	$\mathbf{0.96 \pm 0.01}$	$\mathbf{15.98 \pm 0.01}$

Notes. For explanations about parameters, abbreviations, their unit, and the symbol * refer to the caption below Table 1.
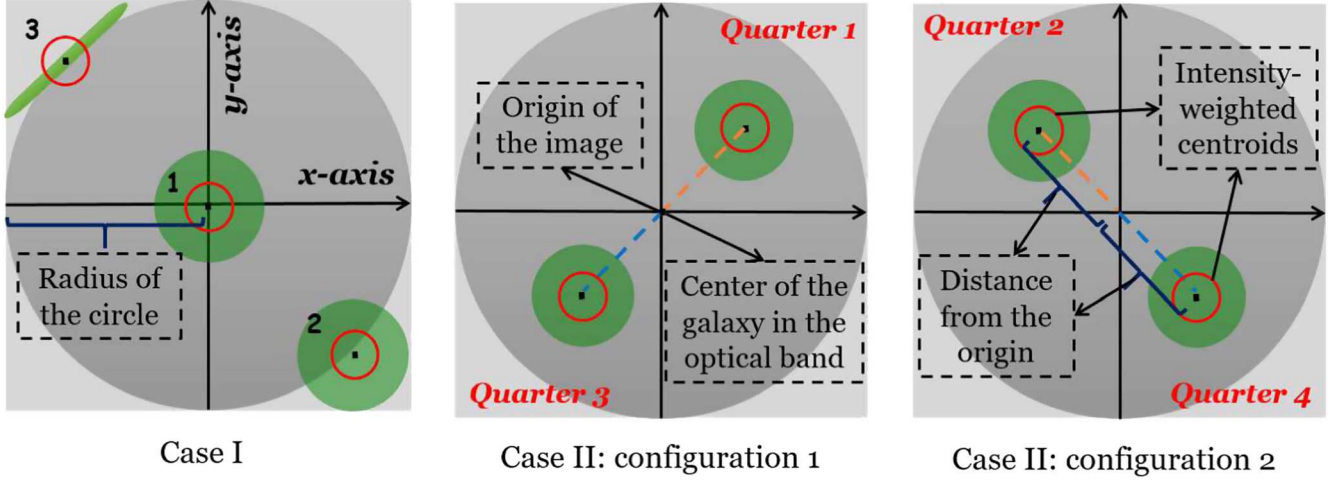
Figure 14. Artificial images including green objects (mimicking the segments of radio galaxies) in different quarters. In Case I, we deal with one segment. The left-side image shows three different segments that can be found in a galaxy map. As seen, segment 1 is a circle whose centroid (the dot in the red circle) is placed in the center of the image. Since both $\mathcal{S}_{\mathrm{proximity}}$ and $\mathcal{S}_{\mathrm{eccentricity}}$ take values of 1, the multiplication of symmetries gives $\mathcal{S} = 1$. Segment 2 is a circle ($\mathcal{S}_{\mathrm{eccentricity}} = 1$) whose centroid position is out of the circumference of interest ($\mathcal{S}_{\mathrm{proximity}} = 0$). In segment 3, both $\mathcal{S}_{\mathrm{proximity}}$ and $\mathcal{S}_{\mathrm{eccentricity}}$ are equal to 0. The two right-side images show the configurations of two segments in Case II with the condition of $\mathcal{S}_{\mathrm{quarter}} = 1$. The distances of the centroids from the origin are displayed with orange and blue dashed lines. Since the dashed lines have the same length, the definition of $\mathcal{S}_{\mathrm{proximity}}$ in Case II leads to a value of 1 for these two configurations.
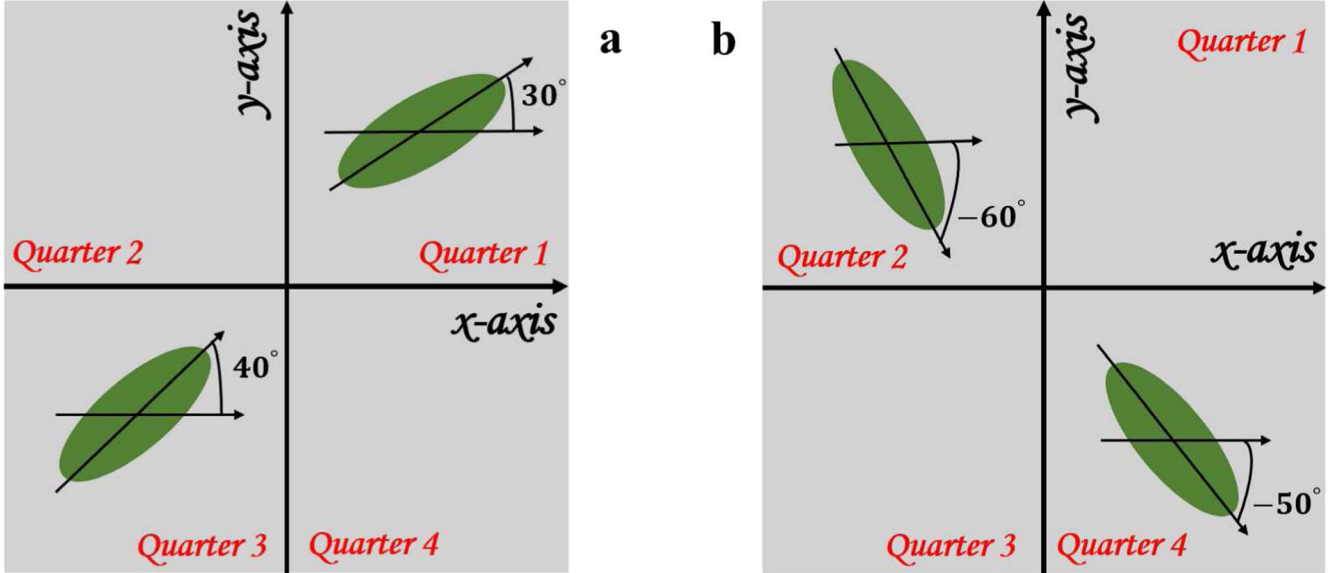
Figure 15. (a) An artificial image including two green objects (mimicking a radio galaxy with two segments) in quarters one and three. The object in quarter one has an orientation of 30° (the angle between the major axis of the object as an ellipse and the positive x-axis), and the object in quarter three has an orientation of 40°. (b) A counterclockwise 90° rotation of plot (a). The object in quarter two has an orientation of −60° (the angle between the major axis of the object as an ellipse and the positive x-axis), and the object in quarter four has an orientation of −50°. We see that the objects in the two quarters in plots (a) and (b) satisfy the condition $|q' - q''| = 2$ (i.e., $|1 - 3| = 2$ and $|2 - 4| = 2$, respectively); so, $\mathcal{S}_{\mathrm{quarter}} = 1$. Furthermore, $\mathcal{S}_{\mathrm{orientation}} = \frac{90 - |\omega_{q'} - \omega_{q''}|}{90}$ is computed as $\frac{90 - |30 - 40|}{90} = 0.8\overline{8}$ and $\frac{90 - |-60 - (-50)|}{90} = 0.8\overline{8}$ for panels (a) and (b), respectively. Thus, for these configurations of the regions in both plots, $\mathcal{S}_{\mathrm{quarter}} \times \mathcal{S}_{\mathrm{orientation}} = 0.8\overline{8}$.
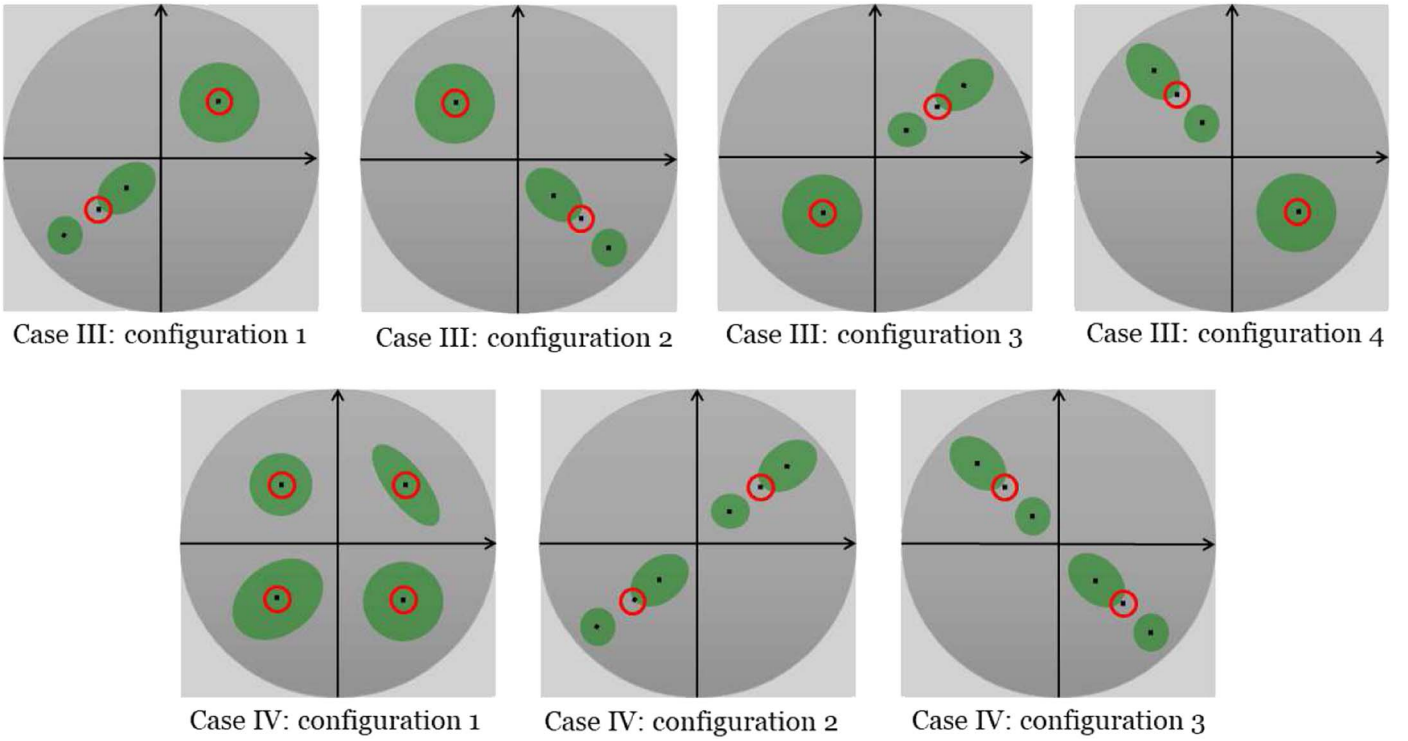
Figure 16. Artificial images including green objects (mimicking the segments of radio galaxies) in different quarters. The upper row shows four configurations of positioning for three segmented regions in radio maps satisfying the condition of $\mathcal{S}_{quarter} = 1$. The lower row shows three configurations of images with four segments satisfying the condition of $\mathcal{S}_{quarter} = 1$. For the two segments in one quarter, the centroids of these two segments (the dots in the red circles) are considered in computations for Cases III and IV.

intensity centroid of the shape as illustrated in Figure 15). Also, all obtained angles are in the range $[-90, 90]$ as noted in Section 3.3. Now, we can discuss orientation-based symmetry $\mathcal{S}_{orientation}$ for two regions that appeared in two different quarters. If two regions are oriented at the same angles, then $\mathcal{S}_{orientation} = 1$. On the other hand, if the bending angle between two regions is $90°$, the symmetry in orientation achieves a minimum value, i.e., $\mathcal{S}_{orientation} = 0$. In a similar way for achieving $\mathcal{S}_{proximity}$ and $\mathcal{S}_{eccentricity}$, the formula $\frac{90 - |\omega_{q'} - \omega_{q''}|}{90}$ gives $\mathcal{S}_{orientation}$, wherein $\omega_{q'}$ and $\omega_{q''}$ are the orientations of the regions in quarters q' and q'', respectively. As it is shown in Figure 15, the value of $\mathcal{S}_{orientation}$ is not affected by the spatial orientation of the recorded image (displacement of coordinate axes). Finally, the multiplication of all these parameters gives the symmetry criterion for two regions as $\mathcal{S} = \mathcal{S}_{quarter} \times \mathcal{S}_{proximity} \times \mathcal{S}_{eccentricity} \times \mathcal{S}_{orientation}$. As an example, we analyze the symmetry parameters for the radio galaxy with ID number 1 (see Table 1) in the FIRST data. Since $|2 - 4| = 2$, $\mathcal{S}_{quarter} = 1$. For an image size of 167^2 pixels, the parameters $\mathcal{S}_{proximity}$, $\mathcal{S}_{eccentricity}$, and $\mathcal{S}_{orientation}$ are computed as $\frac{(167/2) - |12.10 - 21.32|}{(167/2)}$, $\frac{1 - |0.98 - 0.92|}{1}$, and $\frac{90 - |-37.91 - (-42.64)|}{90}$, respectively. Thus, the multiplication of these parameters (i.e., $1 \times 0.89 \times 0.94 \times 0.95$) gives $\mathcal{S} \simeq 0.80$.

Case III: this corresponds to radio maps with three segmented regions. In this case, just one system of positioning regions is admitted: two regions in the same quarter, and the third one in another quarter providing that $|q' - q''| = 2$ (Figure 16, upper row). Now, we find the centroid and the means of the eccentricities and orientations of two segments in one quarter. In this step, we can proceed like in the previous

case. Thus, we can say $\mathcal{S}_{quarter} = 1$; otherwise, $\mathcal{S}_{quarter} = 0$. An example that satisfies this criterion is the radio galaxy with ID number 15 in the LoTSS data (see Table 1), which has three segregated regions within two quarters: one region in the first quarter and two regions in the third quarter. Since $|1 - 3| = 2$, $\mathcal{S}_{quarter} = 1$. In the next step, we must compute the centroid of the two weighted centroids of the two regions in the same quarter (Figure 16, the dots in the red circles). Thus, we can compare the distances of the two centroids from the center of the image in quarters 1 and 3. Now, we can proceed exactly like the previous case for finding $\mathcal{S}_{proximity}$. $\mathcal{S}_{eccentricity}$ and $\mathcal{S}_{orientation}$ are calculated by the means of the eccentricities and the orientations of the regions, respectively, that are in the same quarter. Then, the obtained values are compared with the eccentricities and orientations of the region in the other quarter, respectively. Thus, we can also define a symmetry criterion for such positioning of three regions in a radio map using the last relation given in Case II for the two regions.

Case IV: this corresponds to radio maps with four segmented regions. Figure 16 (lower row) demonstrates three configurations of Case IV satisfying the condition of $\mathcal{S}_{quarter} = 1$. Among the different types of positioning for four regions in a radio map, we are able to define symmetry criteria in just two systems of positioning. In the first type of positioning, each quarter comprises a region of four segmented ones (Figure 16, lower row, configuration 1). Then, for the two regions whose quarters satisfied the condition $|q' - q''| = 2$, we proceed based on Case II. Thus, the requirements of symmetry must be satisfied only for two regions that face each other concerning the optical center. In the second type, two regions are in the same quarter, and the other ones are in another quarter

Table 3
Obtained Values for the Symmetry ($\mathcal{S}$) of FRI Radio Galaxies in the FIRST (F) and LoTSS (L) Data

ID	$\mathcal{S}_F$	$\mathcal{S}_L$	ID	$\mathcal{S}_F$	$\mathcal{S}_L$	ID	$\mathcal{S}_F$	$\mathcal{S}_L$	ID	$\mathcal{S}_F$	$\mathcal{S}_L$
1	0.80	0.83	10	0.04	0.01	19	0.05	0.12	28	0.36	0.07
2	0.03	0.04	11	0.01	0.02	20	0.13	0.13	29	0.12	0.04
3	0.37	0.07	12	0.04	0.11	21	0.24	0	30	0.05	0.05
4	0.07	0.06	13	0.03	0.02	22	0.05	0.04	31	0.05	0.08
5	0.05	0.07	14	0	0	23	0.17	0.03	32	0.10	0.16
6	0.96	0.03	15	0	0.67	24	0	0	33	0.66	0.58
7	0.03	0.02	16	0.02	0.04	25	0.03	0.05	34	0.09	0.13
8	0.16	0.18	17	0.24	0	26	0.47	0.02			
9	0.13	0.14	18	0.09	0	27	0	0			

Note. The mean value of $\mathcal{S}_F$ equals 0.17 ± 0.04; the value for $\mathcal{S}_L$ is obtained to be 0.11 ± 0.03.

Table 4
Obtained Values for the Symmetry ($\mathcal{S}$) of FRII Radio Galaxies in the FIRST (F) and LoTSS (L) Data

ID	$\mathcal{S}_F$	$\mathcal{S}_L$	ID	$\mathcal{S}_F$	$\mathcal{S}_L$	ID	$\mathcal{S}_F$	$\mathcal{S}_L$	ID	$\mathcal{S}_F$	$\mathcal{S}_L$
35	0.11	0.22	44	0	0.39	53	0.88	0.70	62	0.29	0.13
36	0.21	0.29	45	0.10	0.14	54	0.11	0.14	63	0.02	0.05
37	0.39	0.10	46	0.05	0.07	55	0.17	0.20	64	0.15	0.24
38	0.09	0.10	47	0.03	0.06	56	0.07	0.13	65	0.77	0.01
39	0.82	0.63	48	0.46	0.03	57	0.15	0	66	0.04	0.07
40	0.12	0.16	49	0.17	0.18	58	0.14	0.15	67	0.04	0.05
41	0.19	0.27	50	0.05	0.11	59	0.03	0.08			
42	0.53	0.31	51	0.12	0.11	60	0.03	0.06			
43	0.13	0.20	52	0.15	0.25	61	0.39	0.07			

Note. The mean value of $\mathcal{S}_F$ equals 0.21 ± 0.04; the value for $\mathcal{S}_L$ is obtained to be 0.17 ± 0.03.

providing that $|q' - q''| = 2$. Then, as explained in the previous case for two regions in a quarter, we do all those tasks for two regions in two quarters. Finding the centroids and means of the eccentricities and orientations of the regions placed in each quarter and then comparing all obtained parameters like Case II gives the symmetry criterion (Figure 16, lower row, configurations 2 and 3).

In Table 3, we presented a value for the symmetry of region (s) in each FRI image of the FIRST ($\mathcal{S}_F$) and LoTSS ($\mathcal{S}_L$) data sets. Table 4 also provides a value for the symmetry of region (s) in each FRII image of both data sets. The images of 47 radio galaxies in the FIRST data (representing approximately 70% of all data) and for 53 radio galaxies in the LoTSS data (representing approximately 79% of all data) are segmented into a single region. The mean of the symmetry for images containing one region in the FIRST data is determined to be 0.11; this value for images containing one region in the LoTSS data is obtained to be 0.11. The images of 16 radio galaxies in the FIRST data (representing approximately 24% of all data) and nine radio galaxies in the LoTSS data (representing approximately 13% of all data) are segmented into two regions. The mean of the symmetry for the images containing two regions in the FIRST data is computed to be 0.39; this value for the images containing two regions in the LoTSS data equals 0.32. The remaining images with three or four segmented regions have mean symmetries lower than those obtained for images with one or two segmented regions. Notably, the galaxy with the highest symmetry value is a type 2 galaxy (ID = 53) including two segmented regions with symmetries of 0.88 in the FIRST data and 0.70 in the LoTSS data.

5. Summary and Conclusions

The complexities and detailed structures observed in the morphologies of radio galaxies lead us to revisit the classical classification methods. In this regard, improving the sensitivity and resolution of radio observations with the new generation surveys such as LoTSS (Shimwell et al. 2017), the MeerKAT International GHz Tiered Extragalactic Exploration survey (MIGHTEE; Jarvis et al. 2016), the GaLactic and Extragalactic All-sky MWA survey (GLEAM; Wayth et al. 2015), the Evolutionary Map of the Universe (EMU; Norris et al. 2021), and finally the Square Kilometer Array will enable us to identify low surface brightness features and substructures in the morphologies of extended radio galaxies. Therefore, the need for introducing new automatic methods to extract these properties and update the classifications is inevitable. Our first attempt to define a parameter to present the symmetry of a radio galaxy is summarized in this paper.

The framework of this article consists of four significant tasks in image analysis of radio galaxies. First, an automatic flexible method was introduced to denoise and segment the different parts of FRI and FRII radio galaxies in both the FIRST and LoTSS data sets with different resolutions and passbands. Second, by applying the proposed segmentation code that included a histogram-based procedure and the k-means clustering algorithm to galaxy maps, the morphological parameters of segmented regions are extracted. The frequency distributions of size, eccentricity, orientation, and their relationships were studied. Third, we presented a comparison between the results of the FIRST and LoTSS data to analyze and clarify the differences in outputs. Finally, we defined morphological-based criteria for different cases to tackle the problem of finding symmetry.

The results of the morphological analysis showed that the size distributions of various segments of galaxies follow a power-law model with exponents of -0.39 ± 0.06 and -0.55 ± 0.05 for the FIRST and LoTSS data, respectively. These exponents indicate that the sizes of the segmented regions have scale-free behavior. This suggests that the size of galaxies is the result of a self-similar system. Moreover, we found that the contribution of small-scale structures in the LoTSS data is more than those detected in the FIRST data, which can be related to the resolution and/or passband of LoTSS data. According to the eccentricity distribution, it is clear that a vast amount of segmented regions with $\varepsilon > 0.7$ appeared in the form of elongated shapes in galaxy maps. In addition, we found type 1 radio galaxies have on average higher eccentricities than type 2 radio galaxies. The relationship between the sizes of galaxies and their eccentricities shows gradual growth in its scatter plot.

We itemized different cases of galaxies depending on the number of segments in their image tiles to define the symmetry parameter $\mathcal{S}$. Then, the morphological properties of proximity to the center of the image, eccentricity, orientation, and the quarter of the segmented region are considered when calculating $\mathcal{S}$. Among the 67 galaxies in both data sets, the maximum values for $\mathcal{S}$ in the FIRST and LoTSS data are obtained to be 0.88 and 0.70, respectively. They belong to an FRII galaxy with two segmented regions which satisfy the primary condition of $|q' - q''| = 2$. The mean value of symmetry obtained for FRII galaxies is higher than that obtained for FRI galaxies.

This result hints at a relationship between the defined symmetry parameter and the traditional view that existed in the classification of radio galaxies. Although the definition of symmetry is independent of the FR class of radio galaxies, we could use this parameter alongside the FR classification. The symmetry gives a basic description of the morphologies of radio galaxies for less-resolved sources, while this task is impossible in the traditional classification. On the other hand, the coverage of so many details in the definition of this parameter could also provide an effective tool for processing upcoming high-quality radio images.

In future work, we aim to compute $\mathcal{S}$ for a larger sample of radio galaxies using the LoTSS data set. We intend to investigate the relationship between the defined symmetry and other properties of radio galaxies when the data were available (Best et al. 2023). This type of analysis gives a comprehensive understanding of the morphologies of galaxies, and also offers new insights into their classifications. Other interesting work can be exploring the intensity functionality of segments along their major axes. This helps to find a model for simulating galaxies in mock image data and comparing them with original data using supervised (e.g., support vector machine) and/or unsupervised (e.g., artificial neural network) methods.

Appendix

The error range of orientation can be derived by the error propagation method (Noori et al. 2019), which is as follows

$$
\Delta\omega(\mu_{11}, \mu_{20}, \mu_{02})
= \pm \sqrt{\left(\Delta\mu_{11}\frac{\partial\omega}{\partial\mu_{11}}\right)^2 + \left(\Delta\mu_{20}\frac{\partial\omega}{\partial\mu_{20}}\right)^2 + \left(\Delta\mu_{02}\frac{\partial\omega}{\partial\mu_{02}}\right)^2},
\tag{9}
$$

where the error of moments is calculated by $\Delta\mu_{rs} = \pm \sqrt{\left(\Delta x\frac{\partial\mu_{rs}}{\partial x}\right)^2 + \left(\Delta y\frac{\partial\mu_{rs}}{\partial y}\right)^2}$. Since the resolution of the images equals one pixel (i.e., $\Delta x = \Delta y = 1$), by taking $X = (x - X_{\mathrm{IWC}})$ and $Y = (y - Y_{\mathrm{IWC}})$, the errors of moments are obtained

$$
\begin{aligned}
\Delta\mu_{11} &= \pm\sqrt{(\Sigma_X X^2 F^2(x, y)) + (\Sigma_Y Y^2 F^2(x, y))}, \\
\Delta\mu_{20} &= \pm\sqrt{(\Sigma_X 4X^2 F^2(x, y))}, \\
\Delta\mu_{02} &= \pm\sqrt{(\Sigma_Y 4Y^2 F^2(x, y))}.
\end{aligned}
\tag{10}
$$

The partial derivatives of Equation (9) are as follows

$$
\begin{aligned}
\frac{\partial\omega}{\partial\mu_{11}} &= \frac{\mu_{20} - \mu_{02}}{(\mu_{20} - \mu_{02})^2 + 4\mu_{11}^2}, \\
\frac{\partial\omega}{\partial\mu_{20}} &= \frac{-\mu_{11}}{(\mu_{20} - \mu_{02})^2 + 4\mu_{11}^2}, \\
\frac{\partial\omega}{\partial\mu_{02}} &= \frac{\mu_{11}}{(\mu_{20} - \mu_{02})^2 + 4\mu_{11}^2}.
\end{aligned}
\tag{11}
$$

In the same manner, we calculate the error of eccentricity as follows

$$
\begin{aligned}
\Delta\varepsilon(a, b) &= \pm\sqrt{\left(\Delta a\frac{\partial\varepsilon}{\partial a}\right)^2 + \left(\Delta b\frac{\partial\varepsilon}{\partial b}\right)^2}, \\
&= \pm\sqrt{\left(\frac{b^2}{a^4\varepsilon^2}\right)\left(1 + \frac{b^2}{a^2}\right)}.
\end{aligned}
\tag{12}
$$

ORCID iDs

Mohsen Javaherian ● https://orcid.org/0000-0003-0464-1561
Halime Miraghaei ● https://orcid.org/0000-0003-1829-9402
Hooman Moradpour ● https://orcid.org/0000-0003-0941-8422

References

Alegre, L., Sabater, J., Best, P., et al. 2022, MNRAS, 516, 4716
An, F. X., Stach, S. M., Smail, I., et al. 2018, ApJ, 862, 101

Aniyan, A. K., & Thorat, K. 2017, ApJS, 230, 20
Arish, S., Javaherian, M., Safari, H., & Amiri, A. 2016, SoPh, 291, 1209
Arshakian, T. G., & Longair, M. S. 2000, MNRAS, 311, 846
Augusto, P., Gonzalez-Serrano, J. I., Perez-Fournon, I., & Wilkinson, P. N. 2006, MNRAS, 368, 1411
Baldi, R. D., Capetti, A., & Giovannini, G. 2015, A&A, 576, A38
Banhatti, D. G. 1980, A&A, 84, 112
Barkus, B., Croston, J. H., Piotrowska, J., et al. 2022, MNRAS, 509, 1
Baum, S. A., & Heckman, T. 1989, ApJ, 336, 681
Baum, S. A., Heckman, T. M., & van Breugel, W. 1992, ApJ, 389, 208
Baum, S. A., Zirbel, E. L., & O'Dea, C. P. 1995, ApJ, 451, 88
Becker, R. H., White, R. L., & Helfand, D. J. 1995, ApJ, 450, 559
Bera, S., Pal, S., Sasmal, T. K., & Mondal, S. 2020, ApJS, 251, 9
Best, P. N., & Heckman, T. M. 2012, MNRAS, 421, 1569
Best, P. N., Kondapally, R., Williams, W. L., et al. 2023, MNRAS, 523, 1729
Blanton, E. L., Gregg, M. D., Helfand, D. J., Becker, R. H., & Leighly, K. M. 2001, AJ, 121, 2915
Blanton, E. L., Gregg, M. D., Helfand, D. J., Becker, R. H., & White, R. L. 2000, ApJ, 531, 118
Bridle, A. H., Hough, D. H., Lonsdale, C. J., Burns, J. O., & Laing, R. A. 1994, AJ, 108, 766
Cegłowski, M., Gawroński, M. P., & Kunert-Bajraszewska, M. 2013, A&A, 557, A75
Clauset, A., Shalizi, C. R., & Newman, M. E. J. 2009, SIAMR, 51, 661
Condon, J. J., Cotton, W. D., Greisen, E. W., et al. 1998, AJ, 115, 1693
Croston, J. H., Hardcastle, M. J., Mingo, B., et al. 2019, A&A, 622, A10
Dehghan, S., Johnston-Hollitt, M., Franzen, T. M. O., Norris, R. P., & Miller, N. A. 2014, AJ, 148, 75
Dennett-Thorpe, J., Bridle, A. H., Laing, R. A., & Scheuer, P. A. G. 1999, MNRAS, 304, 271
Donoho, D. 1995, ITIT, 41, 613
Donoho, D. L., & Johnstone, I. M. 1994, Biometrika, 81, 425
Fanaroff, B. L., & Riley, J. M. 1974, MNRAS, 167, 31P
Gawroński, M. P., Marecki, A., Kunert-Bajraszewska, M., & Kus, A. J. 2006, A&A, 447, 63
Gendre, M. A., Best, P. N., & Wall, J. V. 2010, MNRAS, 404, 1719
Gendre, M. A., Best, P. N., Wall, J. V., & Ker, L. M. 2013, MNRAS, 430, 3086
Golden-Marx, E., Blanton, E. L., Paterno-Mahler, R., et al. 2021, ApJ, 907, 65
Gopal-Krishna, & Wiita, P. J. 2000, A&A, 363, 507
Gopal-Krishna, & Wiita, P. J. 2004, arXiv:astro-ph/0409761
Govoni, F., Falomo, R., Fasano, G., & Scarpa, R. 2000, A&A, 353, 507
Gupta, V., Mahle, R., & Shriwas, R. S. 2013, in 2013 Tenth Int. Conf. on Wireless and Optical Communications Networks (WOCN) (New York: IEEE), 1
Hamada, A., Asikainen, T., Virtanen, I., & Mursula, K. 2018, SoPh, 293, 71
Hardcastle, M., & Croston, J. 2020, NewAR, 88, 101539
Hardcastle, M. J., & Krause, M. G. H. 2014, MNRAS, 443, 1482
Harwood, J. J., Vernstrom, T., & Stroe, A. 2020, MNRAS, 491, 803
Heckman, T. M., & Best, P. N. 2014, ARA&A, 52, 589
Heckman, T. M., O'Dea, C. P., Baum, S. A., & Laurikainen, E. 1994, ApJ, 428, 65

Hill, G. J., & Lilly, S. J. 1991, ApJ, 367, 1
Hocuk, S., & Barthel, P. D. 2010, A&A, 523, A9
Inbarani, H., Azar, A. T., & Azar, G. J. 2020, J. Electron., 9, 188
Jarvis, M., Taylor, R., Agudo, I., et al. 2016, in Proc. MeerKAT Science: On the Pathway to the SKA (Trieste: SISSA), 6
Javaherian, M., Safari, H., Dadashi, N., & Aschwanden, M. J. 2017, SoPh, 292, 164
Jimenez-Gallardo, A., Massaro, F., Capetti, A., et al. 2019, A&A, 627, A108
Kaiser, C. R., & Best, P. N. 2007, MNRAS, 381, 1548
Khan, S. S., & Ahmad, A. 2004, PaReL, 25, 1293
Krista, L. D., & Gallagher, P. T. 2009, SoPh, 256, 87
Laing, R. A., & Bridle, A. H. 2014, MNRAS, 437, 3405
Laing, R. A., Parma, P., de Ruiter, H. R., & Fanti, R. 1999, MNRAS, 306, 513
Lara, L., Giovannini, G., Cotton, W. D., et al. 2004, A&A, 421, 899
Lukic, V., Brüggen, M., Banfield, J. K., et al. 2018, MNRAS, 476, 246
Mazoochi, F., Miraghaei, H., & Riazi, N. 2022, PASA, 39, e021
Mingo, B., Croston, J. H., Hardcastle, M. J., et al. 2019, MNRAS, 488, 2701
Miraghaei, H., & Best, P. N. 2017, MNRAS, 466, 4346
Moradhaseli, M. A., Javaherian, M., Fathalian, N., & Safari, H. 2021, AcA, 71, 163
Mosavi, S. A. B., Javaherian, M., Sadeghi, M., & Miraghaei, H. 2021, Int. J. Intell. Eng. Syst., 14, 220
Mostert, R. I. J., Duncan, K. J., Röttgering, H. J. A., et al. 2021, A&A, 645, A89
Noori, M., Javaherian, M., Safari, H., & Nadjari, H. 2019, AdSpR, 64, 504
Norris, R. P., Marvil, J., Collier, J. D., et al. 2021, PASA, 38, e046
O'Brien, A. N., Tothill, N. F. H., Norris, R. P., & Filipović, M. D. 2016, arXiv:1602.01914
O'Dea, C. P., & Saikia, D. J. 2021, A&ARv, 29, 3
Raju, K. P., & Bromage, B. J. I. 2006, A&A, 446, 295
Readhead, A. C. S., Taylor, G. B., Pearson, T. J., & Wilkinson, P. N. 1996a, ApJ, 460, 634
Readhead, A. C. S., Taylor, G. B., Xu, W., et al. 1996b, ApJ, 460, 612
Rudnick, L. 2021, Galax, 9, 85
Sadeghi, M., Javaherian, M., & Miraghaei, H. 2021, AJ, 161, 94
Scarpa, R., & Urry, C. M. 2001, ApJ, 556, 749
Schoenmakers, A. P., de Bruyn, A. G., Röttgering, H. J. A., van der Laan, H., & Kaiser, C. R. 2000, MNRAS, 315, 371
Shimwell, T. W., Röttgering, H. J. A., Best, P. N., et al. 2017, A&A, 598, A104
Shimwell, T. W., Tasse, C., Hardcastle, M. J., et al. 2019, A&A, 622, A1
Stucki, K., Solanki, S. K., Schühle, U., et al. 2000, A&A, 363, 1145
Tajik, Z., Javaherian, M., Daei, F., et al. 2023, AdSpR, 72, 1884
Tang, H., Scaife, A. M. M., & Leahy, J. P. 2019, MNRAS, 488, 3358
Taylor, G. B., Readhead, A. C. S., & Pearson, T. J. 1996a, ApJ, 463, 95
Taylor, G. B., Vermeulen, R. C., Readhead, A. C. S., et al. 1996b, ApJS, 107, 37
van Haarlem, M. P., Wise, M. W., Gunst, A. W., et al. 2013, A&A, 556, A2
Wayth, R. B., Lenc, E., Bell, M. E., et al. 2015, PASA, 32, e025
Wedemeyer-Böhm, S., & Rouppe van der Voort, L. 2009, A&A, 503, 225
Yousefzadeh, M., Javaherian, M., & Safari, H. 2015, Iran. J. Astron. Astrophys., 2, 69